Nature of the many-body excitations in a quantum wire: Theory and experiment

O. Tsyplyatyev,[1] A. J. Schofield,[2] Y. Jin,[3] M. Moreno,[3] W. K. Tan,[3] A. S. Anirban,[3] C. J. B. Ford,[3] J. P. Griffiths,[3] I. Farrer,[3] G. A. C. Jones,[3] and D. A. Ritchie[3]

[1]*Institut für Theoretische Physik, Universität Frankfurt, Max-von-Laue Strasse 1, 60438 Frankfurt, Germany*
[2]*School of Physics and Astronomy, University of Birmingham, Birmingham, B15 2TT, United Kingdom*
[3]*Cavendish Laboratory, University of Cambridge, J J Thomson Avenue, Cambridge, CB3 0HE, United Kingdom*

(Received 28 August 2015; revised manuscript received 18 January 2016; published 24 February 2016; corrected 9 March 2016)

The natural excitations of an interacting one-dimensional system at low energy are the hydrodynamic modes of a Luttinger liquid, protected by the Lorentz invariance of the linear dispersion. We show that beyond low energies, where the quadratic dispersion reduces the symmetry to Galilean, the main character of the many-body excitations changes into a hierarchy: calculations of dynamic correlation functions for fermions (without spin) show that the spectral weights of the excitations are proportional to powers of $\mathcal{R}^2/L^2$, where $\mathcal{R}$ is a length-scale related to interactions and L is the system length. Thus only small numbers of excitations carry the principal spectral power in representative regions on the energy-momentum planes. We have analyzed the spectral function in detail and have shown that the first-level (strongest) excitations form a mode with parabolic dispersion, like that of a renormalized single particle. The second-level excitations produce a singular power-law line shape to the first-level mode and multiple power laws at the spectral edge. We have illustrated a crossover to a Luttinger liquid at low energy by calculating the local density of states through all energy scales: from linear to nonlinear, and to above the chemical potential energies. In order to test this model, we have carried out experiments to measure the momentum-resolved tunneling of electrons (fermions with spin) from/to a wire formed within a GaAs heterostructure. We observe a well-resolved spin-charge separation at low energy with appreciable interaction strength and only a parabolic dispersion of the first-level mode at higher energies. We find a structure resembling the second-level excitations, which dies away rapidly at high momentum in line with the theoretical predictions here.

DOI: 10.1103/PhysRevB.93.075147

I. INTRODUCTION

Predicting the behavior of interacting electrons is a significant open problem. Most progress to date has been made at low energies where the linearization of the single-particle dispersion led to the construction of Fermi [1] and, in one dimension, to Luttinger-liquid theories [2] in which the natural excitations are fermionic quasiparticles and hydrodynamic modes, respectively. The only significant progress beyond the linear approximation has been achieved via the heavy impurity model, for Fermi [3–5] and Luttinger [6] liquids, showcasing threshold singularities drastically different from the low-energy behavior. In this paper, we investigate one-dimensional (1D) fermions beyond the linear approximation where the natural many-body excitations form a hierarchical structure, which we have recently discovered [7], in sharp contrast with the Fermi quasiparticles or hydrodynamic modes. We obtain the dynamical structure factor, in addition to the already known spectral function, and construct an inductive proof for calculating the form factors that are necessary for the dynamical response functions of the spinless fermion model. Experimentally, we demonstrate control over the interaction energy a 1D wire manifested as a change of the ratio of the charge and spin velocities at low-energy scales. We find a new structure resembling the second-level excitations, which dies rapidly away from the first-level mode in a manner consistent with a power law.

We analyze theoretically the dynamic response functions—that probe the many-body excitations—for spinless fermions with short-range interactions. Our approach is exact diagonalization via Bethe ansatz methods: the eigenenergies are evaluated in the coordinate representation and form factors—for the corresponding eigenstates—are derived in the algebraic representation, via Slavnov's formula [8]. On the microscopic level, the excitations arrange themselves into a hierarchy via their spectral weights—given by the form factors—with different powers of $\mathcal{R}^2/L^2$, where $\mathcal{R}$ is the

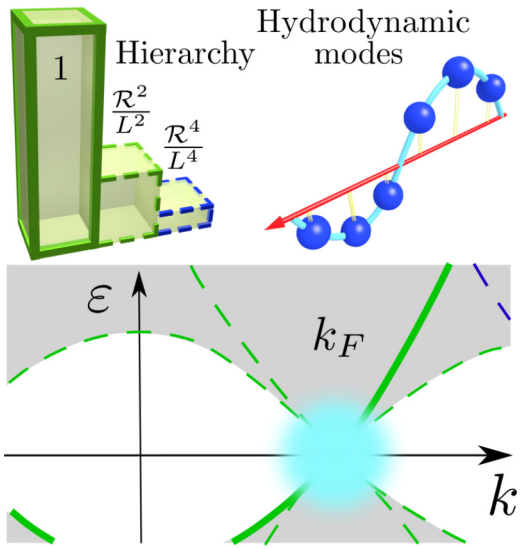

FIG. 1. Regions of the energy-momentum plane dominated by two different principal regimes of the system (bottom): hydrodynamic modes of the Luttinger liquid (top right) at low energies (marked with cyan color in the bottom panel) and the hierarchy of modes (top left) in the rest of the plane.

particle-particle interaction radius and L is the length of the system. As a result, only small numbers of states—out of an exponentially large Fock space of the many-body system—carry the principal spectral power in representative regions on the energy-momentum plane, see Fig. 1, allowing an analytical evaluation of the observables.

At small energy, this hierarchy crosses over to a hydrodynamic behavior, see Fig. 1, which we illustrate by calculating the local density of states. At low energy, it is suppressed in a power-law fashion according to the Tomonaga-Luttinger theory. Away from the Fermi point where the Lorentz invariance is reduced to Galilean by the parabolicity of the spectrum, the local density of states is dominated by the first(leading)-level excitations of the hierarchy. This produces a $1/\sqrt{\varepsilon}$ van Hove singularity, where ε is the energy measured from the bottom of the conduction band. At even higher energies, the second-level excitations produce another $1/\sqrt{|\varepsilon|}$ van Hove singularity on the other side of the band edge, in the forbidden for the noninteracting system region.

Using this framework, we study the response of the correlated system to adding/removing a particle in detail, given by the spectral function. The first-level excitations form a parabolic dispersion, like a single particle, with a mass renormalized by the Luttinger parameter K [9]. The continuous spectrum of the second-level excitations produces a power-law line shape around the first-level mode with a singular exponent -1. Around the spectral edges, the second-level excitations give a power-law behavior of the spectral function. For the hole edge, the exponent calculated microscopically reproduces the prediction of the phenomenological heavy impurity model in one dimension [6]. However, around the particle edge, the second-level excitations give a power-law of a new type.

Experimentally, momentum-resolved tunneling of electrons confined to a 1D geometry has been used to probe spin-charge separation in a Luttinger liquid [11,12,38,39]. This separation was observed to persist far beyond the energy range for which the Luttinger approximation is valid [12], showing the need for more sophisticated theories [37]. Particle-hole asymmetry has also been detected in relaxation processes [10]. In this paper, we measure momentum-resolved tunneling of electrons in the upper layer of a GaAs-AlGaAs double-quantum-well structure from/to a 2D electron gas in the lower layer. This setup probes the spectral function for spinful fermions. We observe a well-resolved spin-charge separation at low energy with appreciable interaction strength—a distinct effect of the spinful generalization of Luttinger liquid [2]. The ratio of charge and spin velocities is $v_c/v_s \approx 1.8$ [12]. At high energy, in addition to the spin and charge curves, we can also resolve the structure just above k_F that appears to be the edge of the second-level excitations. However, the amplitude decays rapidly and for higher k we find no sign of the higher-level excitations, implying that their amplitude must have become at least three orders of magnitude weaker than for the parabola formed by the first-level excitations. The picture emerging out of these experimental results can only be explained—though only qualitatively—by the hierarchy that we study for spinless fermions.

The rest of the paper is organized as follows. In Sec. II, we describe the one-dimensional model of interacting spinless fermions introducing a short-range cutoff via lattice. Section III contains a procedure of finding the many-body eigenenergy by means of the coordinate Bethe ansatz. In Sec. IV, we evaluate the form factors needed for the dynamical response functions. We give a construction of the algebraic representation of the Bethe ansatz (Sec. IV A) and evaluate the scalar product in this representation (Sec. IV B). We present a calculation of the form factors for the spectral function and the dynamical structure factor for a finite chain (Sec. IV C). We take the limit of long wavelengths deriving polynomial formulas for the form factors (Sec. IV d). Then, we analyze the obtained form factors establishing the hierarchy of excitations (Sec. IV e). Finally, we calculate the spectral function around the spectral edges (Sec. IV f). In Sec. V, we illustrate the crossover to a Luttinger liquid at low energy by evaluating the local density of states at all energy scales. Section VI describes experiments on the momentum-conserved tunnelling of electrons in semiconductor wires. Section VII is dedicated to low energies and in Sec. VIII, we analyze the measurements at high energies connecting the experiment with the theory on spinless fermions developed in this paper. The figures below are marked with spinless and spinful logos (such as those in Fig. 2 and 7, respectively) to indicate the structure of the paper visually. Appendix A contains details of the derivation of the Bethe equations in the algebraic representation. In Appendix B, we derive the expectation value of the local density operator.

II. MODEL OF SPINLESS FERMIONS

We study theoretically the model of interacting Fermi particles without spin in 1D,

$$H = \int_{-\frac{L}{2}}^{\frac{L}{2}} dx \left(-\frac{1}{2m}\psi^\dagger(x)\Delta\psi(x) + UL\rho(x)^2 \right), \qquad (1)$$

where the field operators $\psi(x)$ satisfy the Fermi commutation relations, $\{\psi(x),\psi^\dagger(x')\} = \delta(x-x')$, $\rho(x) = \psi^\dagger(x)\psi(x)$ is the particle density operator, and m is the bare mass of a single particle. Below, we consider periodic boundary conditions, $\psi(x+L) = \psi(x)$, restrict ourselves to repulsive interaction $U > 0$ only, and take $\hbar = 1$.

Nonzero matrix elements of the interaction term in Eq. (1) require a finite range of the potential profile for Fermi particles. Here, we will introduce a lattice with next-neighbor interaction whose lattice parameter and interaction radius is $\mathcal{R}$. The model in Eq. (1) becomes

$$H = \sum_{j=-\frac{\mathcal{L}}{2}}^{\frac{\mathcal{L}}{2}} \left[\frac{-1}{2m}(\psi_j^\dagger\psi_{j+1} + \psi_j^\dagger\psi_{j-1}) + U\rho_j\rho_{j+1} \right], \qquad (2)$$

where j is the site index on the lattice, the dimensionless length of the system is $\mathcal{L} = L/\mathcal{R}$, the operators obey $\{\psi_j,\psi_j^\dagger\} = \delta_{ij}$, and $\rho_j = \psi_j^\dagger\psi_j$.

The long-wavelength limit of the discrete model corresponds to the model in Eq. (1), while the interaction radius $\mathcal{R}$ provides microscopically an ultraviolet cutoff in the continuum regime. For the N-particle states of the lattice model, we additionally impose the constraint of low particle density, $N/\mathcal{L} \ll 1$, to stay within the conducting regime; a large

occupancy $N \sim \mathcal{L}$ might lead to Wigner crystal physics at sufficiently strong interactions that would localize the system. This procedure is analogous to the point splitting regularization technique [15], which is usually introduced within the framework of the Luttinger liquid mode in the linear regime.

III. SPECTRAL PROPERTIES

The model in Eq. (2) can be diagonalized via the Bethe ansatz approach, which is based on the observation that the eigenstates are superpositions of plain waves. This method is also called coordinate Bethe ansatz [13]. The eigenstates, following Ref. [13], can be parameterized with sets of N quasimomenta k_j,

$$\Psi = \sum_{\mathcal{P}, j_1<\cdots<j_N} e^{i\sum_l k_{P_l} j_l + i\sum_{l<l'} \varphi_{P_l,P_{l'}}} \psi^\dagger_{j_1} \dots \psi^\dagger_{j_N} |\text{vac}\rangle. \quad (3)$$

Their corresponding eigenenergies, $H\Psi = E\Psi$, are $E = \sum_{j=1}^{N} (1-\cos k_j)/m$. Here, $|\text{vac}\rangle$ is the vacuum state, the scattering phases are fixed by the two-body scattering problem,

$$e^{i2\varphi_{ll'}} = -\frac{e^{i(k_l+k_{l'})} + 1 + 2mUe^{ik_l}}{e^{i(k_l+k_{l'})} + 1 + 2mUe^{ik_{l'}}} \quad (4)$$

and $\sum_{\mathcal{P}}$ is a sum over all permutations of quasimomenta. The periodic boundary condition quantizes the whole set of N quasimomenta simultaneously,

$$\mathcal{L}k_j - 2\sum_{l\neq j} \varphi_{jl} = 2\pi I_j, \quad (5)$$

where I_j are sets of nonequal integer numbers.

Generally, the system of equations in Eq. (5) has to be solved numerically to obtain the full spectral structure of the observables. However, in the long-wavelength regime, the solutions can be evaluated explicitly.

In this limit, the scattering phases in Eq. (4) are linear functions of quasimomenta, $2\varphi_{ll'} = (k_l - k_{l'})/(1+(mU)^{-1}) + \pi$, which makes the nonlinear system of Bethe ansatz equations in Eq. (5) a linear system [9]. Then, solving the linear system for $\mathcal{L} \gg 1$ via the matrix perturbation theory up to the first subleading order in $1/\mathcal{L}$, we obtain

$$k_j = \frac{2\pi I_j}{\mathcal{L} - \frac{mUN}{mU+1}} - \frac{mU}{mU+1} \sum_{l\neq j} \frac{2\pi I_l}{\left(\mathcal{L} - \frac{mUN}{mU+1}\right)^2}. \quad (6)$$

Note that this calculation is valid for any interaction strength at low densities. The corresponding eigenenergy and total momentum (protected by the translational invariance of the system) are

$$E = \sum_j \frac{k_j^2}{2m} \quad (7)$$

and $P = \sum_j k_j$.

The spectrum of the many-body states is governed by the first term in Eq. (6). Reduction of the quantization length in the denominator of the first term in Eq. (6) is an exclusion volume taken by the sum of interaction radii of all particles. Thus all N-particle eigenstates at an arbitrary interaction strength are given straightforwardly by the same sets of integer numbers I_j as the free fermions' states, e.g., the ground state corresponds to $I_j = -N/2, \dots, N/2$.

For example, this result can be used to calculate the low-energy excitations explicitly that define the input parameters of the Luttinger-liquid model, the velocity of the sound wave v and of the Luttinger parameter K. The first pair of the particle-like excitations, when an extra electron is added just above the Fermi energy, have $I_{N+1} = N/2+1$ and $I_{N+1} = N/2+2$. The difference in their energies and momenta are $E_2 - E_1 = (2\pi)^2 N/[2m(\mathcal{L} - \frac{mUN}{mU+1})^2]$ and $P_2 - P_1 = 2\pi/\mathcal{L}$. Evaluating the discrete derivative, which gives the slope of the dispersion around the Fermi energy, as $v = (E_2 - E_1)/(P_2 - P_1)$ we obtain

$$v = \frac{v_F}{\left(1 - \frac{NmU}{\mathcal{L}(1+mU)}\right)^2} \quad \text{and} \quad K = \left(1 - \frac{NmU}{\mathcal{L}(1+mU)}\right)^2, \quad (8)$$

where $v_F = \pi N/(mL)$ is the Fermi velocity and the relation $vK = v_F$ between the Luttinger parameters for Galilean invariant systems [14] was used.

IV. MATRIX ELEMENTS

Now we turn to the calculation of matrix elements. However, first we need to select operators that correspond to specific observables. Our interest lies in the dynamical response functions that correspond to adding/removing a single particle to/from a correlated system and to creating an electron-hole pair excitation out of the ground state of a correlated system. For example, the first type of dynamics can be realized in experiments using semiconductor nanostructures [11,12] where an electrical current, generated by electrons tunneling into/from the nanostructure with their momentum and energy under control, probe the system.

The response of the many-body system to a single-particle excitation at momentum k and energy ε is described by spectral function [16] $A(k,\varepsilon) = -\text{Im}[\int dxdt e^{i(kx-\varepsilon t)} G(x,0,t)]\text{sgn}(\varepsilon-\mu)/\pi$. Here, μ is the chemical potential and $G(x,x',t) = -i\langle T(e^{-iHt}\psi(x)e^{iHt}\psi^\dagger(x'))\rangle$ is the Green function at zero temperature. In terms of the eigenstates, the spectral function reads

$$A(k,\varepsilon) = L\sum_f |\langle f|\psi^\dagger(0)|0\rangle|^2 \delta(\varepsilon - E_f + E_0)\delta(k - P_f) + L\sum_f |\langle 0|\psi(0)|f\rangle|^2 \delta(\varepsilon + E_f - E_0)\delta(k + P_f), \quad (9)$$

where E_0 is the energy of the ground state $|0\rangle$, and P_f and E_f are the momenta and the eigenenergies of the eigenstates $|f\rangle$; all eigenstates are assumed normalized.

The creation of an electron-hole pair out of the correlated state at zero temperature at momentum k and energy ε is described by a dynamical structure factor [16] $S(k,\varepsilon) = \int dxdt e^{i(kx-\varepsilon t)}\langle\rho(x,t)\rho(0,0)\rangle$, where $\rho(x,t) = e^{-iHt}\rho(0)e^{iHt}$ is the density operator evolving under the Hamiltonian to time t and the average $\langle\dots\rangle$ is taken over the ground state. In terms

of the eigenstates, the dynamical structure factor reads

$$S(k,\varepsilon) = L\sum_f |\langle f|\rho(0)|0\rangle|^2\delta(\varepsilon - E_f)\delta(k - P_f). \quad (10)$$

Thus we will be analyzing the expectation values of the local operators $\psi(0)$ and $\rho(0)$. To proceed with this calculation, we will borrow the result from Refs. [17,18] for Heisenberg chains. Our strategy is to perform the full calculation for the discrete model in Eq. (2) obtaining the matrix elements of ψ_j and ρ_j as determinants. Then we will take the long-wavelength limit to evaluate the form factors for the continuum model explicitly, which will be the main technical result in the theoretical part of this paper. Below, we will construct the algebraic form of Bethe ansatz, use the Slavnov's formula [8] to express the scalar product and the normalization factors in this representation, and finally calculate the matrix elements of the local operators.

A. Algebraic Bethe ansatz

The wave functions of the N-particle eigenstates are factorized in the algebraic representation, which allows the general calculation of various scalar products between them. Here, we will follow the construction in Ref. [13] for XXZ spins chains changing basis from 1/2-spins to spinless fermions.

The so-called R matrix acts on a tensor product $V_1 \otimes V_2$ space and depends on an auxiliary parameter u, where V_1 and V_2 are element-element subspaces, each of which consists of two states $|0\rangle_j$ and $|1\rangle_j$. It is a solution of Yang-Baxter equation $R_{12}(u_1 - u_2)R_{13}(u_1)R_{23}(u_2) = R_{23}(u_2)R_{13}(u_1)R_{12}(u_1 - u_2)$. For the lattice model in Eq. (2), the R matrix reads

$$\begin{aligned} R_{12} = 1 &- (1 - b(u))(c_1^\dagger c_1 + c_2^\dagger c_2) \\ &- 2b(u)c_1^\dagger c_1 c_2^\dagger c_2 + c(u)(c_1^\dagger c_2 + c_2^\dagger c_1), \end{aligned} \quad (11)$$

where

$$b(u) = \frac{\sinh(u)}{\sinh(u+2\eta)}, \quad c(u) = \frac{\sinh(2\eta)}{\sinh(u+2\eta)}. \quad (12)$$

Here, η is the interaction parameter, and the tensor product space is defined using a fermionic basis $|0\rangle_j$ and $|1\rangle_j$ with corresponding fermionic operators $\{c_i, c_j^\dagger\} = \delta_{ij}$ that act in these bases as $c_j^\dagger|0\rangle_j = |1\rangle_j$. The latter will account for the anticommuting nature of the lattice fermions on different sites in contrast to the commutation relation of the spin operators of a spin chain model [22,23]. All further calculations are identical to spin chains where the anticommutation relations of the Fermi particles are, however, automatically fulfilled. This approach is more convenient than direct mapping of the results for spin chains using Jordan-Wigner transformation [19].

A two-states subspace of the R matrix can be identified with the two-states fermionic subspace of the lattice site j of the model in Eq. (2). Then, the quantum version of the Lax operator (the so called L matrix) can be defined as $L_j = R_{\xi j}$. In the auxiliary subspace ξ its matrix and operator forms are

$$\begin{aligned} L_j &= \begin{pmatrix} \frac{\cosh(u-\eta(2\rho_j-1))}{\cosh(u-\eta)} & -i\frac{\sinh 2\eta c_j^-}{\cosh(u-\eta)} \\ -i\frac{\sinh 2\eta c_j^\dagger}{\cosh(u-\eta)} & -\frac{\cosh(u+\eta(2\rho_j-1))}{\cosh(u-\eta)} \end{pmatrix} \\ &= A^j(1 - c_\xi^\dagger c_\xi) + c_\xi^\dagger C^j + B^j c_\xi + D^j c_\xi^\dagger c_\xi. \end{aligned} \quad (13)$$

Here, the top left element of the matrix is a transition between $|0\rangle_\xi$ and $\langle 0|_\xi$ states of the auxiliary subspace, c_j and ρ_j are the fermionic operators of the lattice model in Eq. (2), and A^j, B^j, C^j, D^j label the matrix elements of L_j. The prefactor in front of L_j was chosen such that for $u = i\pi/2 - \eta$ it becomes a permutation matrix and for $\eta = 0$ the L operator is diagonal.

By construction, the L operator satisfies the algebra generated by the Yang-Baxter equation,

$$R(u-v)\big(L_j(u) \otimes L_j(v)\big) = \big(L_j(v) \otimes L_j(u)\big)R(u-v). \quad (14)$$

The entries give commutation relations between the matrix elements of L matrix. Here, we write down three of them that will be used later,

$$\big\{B_u^j, C_v^j\big\} = \frac{c(u-v)}{b(u-v)}\big(D_v^j A_u^j - D_u^j A_v^j\big), \quad (15)$$

$$A_u^j C_v^j = \frac{1}{b(v-u)}C_v^j A_u^j - \frac{c(v-u)}{b(v-u)}C_u^j A_v^j, \quad (16)$$

$$D_u^j C_v^j = -\frac{1}{b(u-v)}C_v^j D_u^j + \frac{c(u-v)}{b(u-v)}C_u^j D_v^j. \quad (17)$$

These relations can be also be checked explicitly by direct use of the definition in Eq. (13) and the Fermi commutation relations.

The transition matrix $T(u)$ for a chain with $\mathcal{L}$ sites—the so-called monodromy matrix—can be defined similarly to the classical problem as

$$T(u) = \sum_{j=1}^{\mathcal{L}} L_j(u). \quad (18)$$

If all single-site L matrices satisfy Eq. (14) then the T matrix also satisfies the same Yang-Baxter equation, e.g., see proof in Ref. [13]. Therefore the matrix elements of $T = A(1 - c_\xi^\dagger c_\xi) + c_\xi^\dagger C + Bc_\xi + Dc_\xi^\dagger c_\xi$ in the 2×2 auxiliary space ξ obey the same commutation relations in Eqs. (15)–(17). The transfer matrix for the whole chain,

$$\tau = \mathrm{str}T = A(u) - D(u), \quad (19)$$

is the super trace of T matrix due to the fermionic definition of the auxiliary space [22,23]. The latter gives a family of commuting matrices $[\tau(u), \tau(v)] = 0$, which contain all conserved quantities of the problem including the Hamiltonian.

The vacuum state $|0\rangle$—in the Fock space of the model in Eq. (2)—is an eigenstate of the transfer matrix τ. The corresponding eigenvalue, $\tau(u)|0\rangle = (a(u) - d(u))|0\rangle$, is the difference of the eigenvalues of the A and D operators which can be obtained directly by use of the definitions in Eqs. (13) and (18). Noting that for $\mathcal{L} = 2$ Eq. (18) gives $A(u)|0\rangle = a_1(u)a_2(u)|0\rangle$ and $D(0)|0\rangle = d_1(u)d_2(u)|0\rangle$, where $a_1(u) = a_2(u) = \cosh(u+\eta)/\cosh(u-\eta)$ and $d_1(u) = d_2(u) = 1$,

and generalizing this observation for arbitrary $\mathcal{L}$ one obtains

$$a(u) = \frac{\cosh(u+\eta)^{\mathcal{L}}}{\cosh(u-\eta)^{\mathcal{L}}}, \quad \text{and} \quad d(u) = 1. \tag{20}$$

A general state of N particles'—Bethe state–is constructed by applying the operator $C(u)$ N times with different values of the auxiliary variable u_j,

$$\Psi = \prod_{j=1}^{N} C(u_j)|0\rangle, \tag{21}$$

where a set of N values u_j corresponds to N quasimomenta k_j in coordinate representation of Bethe states in Eq. (3). The state in Eq. (21) with an arbitrary set of u_j is not an eigenstate of the transfer matrix τ. For instance, it can be seen by commuting the operators A and D from left to right through all operators $C(u_j)$ that generates many different states according to the commutation relations in Eqs. (16) and (17). However, the contribution of all of the states that are nondegenerate with Ψ can made to be zero by choosing particular sets of u_j that satisfy the following set of equations

$$\frac{a(u_j)}{d(u_j)} = (-1)^{N-1} \prod_{l=1\neq j}^{N} \frac{b(u_l - u_j)}{b(u_j - u_l)} \tag{22}$$

(see Appendix A for details).

Under the substitution of the vacuum eigenvalues $a(u_j)$ and $d(u_j)$ of A and D operators from Eq. (20) and $b(u_l - u_j)$—which define the commutation relations Eqs. (16) and (17)—from Eq. (12) this so-called eigenvalue equation above becomes

$$\frac{\cosh(u_j-\eta)^{\mathcal{L}}}{\cosh(u_j+\eta)^{\mathcal{L}}} = (-1)^{N-1} \prod_{l=1\neq j}^{N} \frac{\sinh(u_j - u_l - 2\eta)}{\sinh(u_j - u_l + 2\eta)}. \tag{23}$$

Thus all the sets of u_j that satisfy the above equation give eigenstates of the transfer matrix in the representation of Eq. (21) with the corresponding eigenvalues $\tau(u)\Psi = \mathcal{T}(u)\Psi$, where

$$\mathcal{T}(u) = a(u) \prod_{j=1}^{N} \frac{1}{b(u_j - u)} - (-1)^N d(u) \prod_{j=1}^{N} \frac{1}{b(u - u_j)}. \tag{24}$$

This eigenvalue equation in the algebraic framework is the direct analog of the Bethe ansatz equation (5) in the coordinate representation. Direct mapping between the two is done by the substitution of

$$e^{ik_j} = \frac{\cosh(u_j - \eta)}{\cosh(u_j + \eta)}, \quad mU = -\cosh 2\eta, \tag{25}$$

in Eq. (5) and by taking its exponential.

The original lattice Hamiltonian can be obtained from the transfer matrix $\tau(u)$ that contains all of the conserved quantities of the problem. The logarithmic derivatives of $\tau(u)$ give the global conservation laws by means of the so-called trace identities, see Ref. [13]. The linear coefficient in the Taylor series around the point $u = \frac{i\pi}{2} - \eta$ is proportional to the Hamiltonian itself. After restoring the correct prefactor, the expression reads

$$H = -\frac{\sinh\eta}{2m} \partial_u \ln \tau(u)|_{u=\frac{i\pi}{2}-\eta}. \tag{26}$$

Substitution of the interaction parameter η from Eq. (25) in terms of the particle-particle interaction constant U into the right-hand side of the above relation recovers the lattice model in Eq. (2).

B. Scalar product

The basic quantity on which the calculations of the expectation values will be based on is the scalar product of two wave functions. A general way of evaluating it is based on the commutation relations in Eqs. (15)–(17) and the vacuum expectation values of the A and D operators. The result of such a calculation simplifies greatly if one of the Bethe states is an eigenstate of the transfer matrix $\tau(u)$, as was first shown by Slavnov [8]. Then, the same result was rederived in Refs. [17,18] using the so-called factorizing F matrix [20], which is a representation of a Drinfeld twist [21]. The latter will not be used in this section but it will be needed later in calculations of the matrix elements of the local operators.

Let $|\mathbf{u}\rangle = \prod_{j=1}^{N} C(u_j)|0\rangle$ be an eigenstate of the transfer matrix so that N parameters u_j satisfy the Bethe equation in Eq. (23); and let $\langle\mathbf{v}| = \langle 0| \prod_{j=1}^{N} B(v_j)$ be another Bethe state parametrized by a set of N arbitrary values v_j. The scalar product of these two states $\langle\mathbf{v}|\mathbf{u}\rangle$ can be evaluated by commuting each operator $B(v_j)$ through the product of $C(u_j)$ operators using the commutation relation in Eq. (15), which generates the A and D operators with all possible values of u_j and v_j. They, in turn, have also to be commuted to the right through the remaining products of the $C(u_j)$ operators. Finally, products of the A and D operators, which act upon the vacuum state, just give products of their vacuum eigenvalues $a(u_j), d(u_j)$ and $a(v_j), d(v_j)$ according to Eq. (20). The resulting sums of products can be written, using the relation between u_js in Eq. (23), in a compact form as a determinant of an $N \times N$ matrix [8]:

$$\langle\mathbf{v}|\mathbf{u}\rangle = \frac{\prod_{i,j=1}^{N} \sinh(v_j - u_i)}{\prod_{j<i} \sinh(v_j - v_i) \prod_{j<i} \sinh(u_j - u_i)} \det \hat{S}, \tag{27}$$

where the matrix elements are $S_{ab} = \partial_{u_a} \mathcal{T}(v_b)$. Under a substitution of the eigenvalues of the transfer matrix from Eq. (24), these matrix elements read in explicit form as

$$S_{ab} = -\frac{\cosh^L(v_b+\eta)}{\cosh^L(v_b-\eta)} \frac{\sinh(2\eta)}{\sinh^2(u_a - v_b)} \prod_{j=1\neq a}^{N} \frac{\sinh(u_j - v_b + 2\eta)}{\sinh(u_j - v_b)} - (-1)^N \frac{\sinh(2\eta)}{\sinh^2(v_b - u_a)} \prod_{j=1\neq a}^{N} \frac{\sinh(v_b - u_j + 2\eta)}{\sinh(v_b - u_j)}. \tag{28}$$

For $N = 1$, the result in Eqs. (27) and (28) follows directly from Eq. (15). For arbitrary N, the proof is more complicated: it employs the residue formula [8] (the function $\langle\mathbf{v}|\mathbf{u}\rangle$ has first order poles when $v_i \to u_j$) and the recurrent relation for the scalar product of $N+1$ particles in terms of the scalar product of N particles, see also details in Ref. [13].

The normalization factor of Bethe states can be obtained from Eq. (27) by taking the limit $\mathbf{v} \to \mathbf{u}$. The first-order singularities, $(v_b - u_b)^{-1}$, in the off-diagonal matrix elements (28) are canceled by zeros in the numerator in Eq. (27). The diagonal $a = b$ matrix elements contain second-order singularities $(v_b - u_b)^{-2}$ for $\mathbf{v} \to \mathbf{u}$. However, the numerator also becomes zero when $\mathbf{v} \to \mathbf{u}$ in the leading order. Its expansion up to the first subleading order cancels the second-order singularity of the denominator giving a finite expression for the matrix elements in the limit. The normalization factor is found to be

$$\langle \mathbf{u}|\mathbf{u}\rangle = \sinh^N(2\eta) \prod_{i\neq j=1}^{N} \frac{\sinh(u_j - u_i + 2\eta)}{\sinh(u_j - u_i)} \det \hat{Q}, \tag{29}$$

where the matrix elements are

$$Q_{ab} = \begin{cases} -\mathcal{L}\frac{\sinh 2\eta}{\cosh(u_a+\eta)\cosh(u_a-\eta)} - \sum_{j\neq a} \frac{\sinh 4\eta}{\sinh(u_a-u_j-2\eta)\sinh(u_a-u_j+2\eta)}, & a = b, \\ \frac{\sinh 4\eta}{\sinh(u_b-u_a+2\eta)\sinh(u_b-u_a-2\eta)}, & a \neq b. \end{cases} \tag{30}$$

The last formula was originally derived by Gaudin using quantum-mechanical identities in the coordinate representation of Bethe ansatz [24]. Mapping of the resulting expression in Ref. [24] to the algebraic representation by means of Eq. (25) gives directly the result in Eqs. (27) and (28) with a different prefactors due to different normalization factors in the definitions of the states in Eq. (3) and of the states in Eq. (21). We will use the algebraic form in Eq. (21) for the calculation of the local matrix elements below.

C. Expectation values of local operators

Operators of the algebraic Bethe ansatz in Eqs. (13) and (18) are nonlocal in the basis of the original fermionic operators of the lattice model in Eq. (2). Thus the first nontrivial problem in calculating the matrix elements of the local operators $\psi_j^\dagger$ and ρ_1 in the algebraic representation of Bethe states in Eq. (21) is expressing the operators of our interest in terms of the nonlocal A, B, C, and D operators from Eqs. (13) and (18). Alternatively, these Bethe operators can be expressed in terms of the local operators of the lattice model. The latter approach is much more complicated since the product of matrices in Eq. (18) is a large sum (exponential in the number of sites in the chain) restricting severely the ability to do explicit calculations using the fermionic representation in practice.

An alternative way was found by constructing the F-matrix representation of a Drinfeld twist [20]. In the F basis, the monodromy matrix in Eq. (18) becomes quasilocal, i.e., its diagonal elements A and D become direct products of diagonal matrices on each site over all sites of the chain and the off-diagonal B and C are single sums over such direct products. Direct calculations become much easier in this basis. Specifically, analysis of A, B, C, and D operators leads to a simple result for representing the ψ_j operator in terms of algebraic Bethe ansatz operators, which then is shown to be basis independent [17,18],

$$\psi_j^\dagger = \tau^{j-1}\left(\frac{i\pi}{2} - \eta\right) C\left(\frac{i\pi}{2} - \eta\right) \tau^{\mathcal{L}-j}\left(\frac{i\pi}{2} - \eta\right). \tag{31}$$

Here, $\tau(u) = A(u) - D(u)$ is the supertrace of the monodromy matrix and $C(u)$ is its matrix element.

The transfer matrices in the right-hand side of the above equation give only a phase prefactor in the expectation values with respect to the Bethe states in Eq. (21). Let $|\mathbf{u}\rangle$ be an eigenstate of the transfer matrix with N particles, let $|\mathbf{v}\rangle$ be an eigenstate with $N+1$ particles, and let us consider the case of $j = 1$. Acting with the $\tau^{\mathcal{L}-1}(i\pi/2 - \eta)$ operator on the eigenstates $|\mathbf{u}\rangle$ gives the eigenvalue $\prod_{j=1}^N \cosh^{\mathcal{L}-1}(u_j - \eta)/\cosh^{\mathcal{L}-1}(u_j + \eta)$ according to Eq. (24). Then, using the mapping to the coordinate representation in Eq. (25) and the Bethe equation in the form of Eq. (5), this eigenvalue can be expressed as $\exp[i P_u(\mathcal{L} - 1)]$, where P_u is the total momentum of the state u_j, a quantum number. Similar phase factors for $j \neq 1$ are evaluated in an analogous way and each of them cancels out under modulus square in the form factor in Eq. (9) making the local form factors independent of j in full accord with the translational invariance of the system and the observable in Eq. (9). Thus we will only calculate the value of $\langle \mathbf{v}|\psi_1^\dagger|\mathbf{u}\rangle$.

Since $C(\frac{i\pi}{2} - \eta)\prod_{j=1}^N C(u_j)|0\rangle$ is also a Bethe state $|\frac{i\pi}{2} - \eta, u_j\rangle$, though it is not an eigenstate, the expectation value can be calculated using the result for the scalar product $\langle \mathbf{v}|\psi_j^\dagger|\mathbf{u}\rangle = \langle \mathbf{v}|\frac{i\pi}{2} - \eta, u_j\rangle$. Substituting $\frac{i\pi}{2} - \eta, u_j$ in Eqs. (27) and (28) explicitly, one obtains

$$\langle \mathbf{v}|\psi_1^\dagger|\mathbf{u}\rangle = (-1)^{N+1} i \frac{\prod_{j=1}^{N+1}\cosh(v_j - \eta)}{\prod_{j=1}^N \cosh(u_j + \eta)} \times \frac{\sinh^{N+1}(2\eta)\det \hat{M}}{\prod_{j<i=2}^N \sinh(u_j - u_i)\prod_{j<i=2}^{N+1}\sinh(v_j - v_i)}, \tag{32}$$

where the matrix elements are

$$M_{ab} = \frac{(-1)^{N-1}}{\sinh(u_b - v_a)}\left(\prod_{j=1\neq b}^{N} \frac{\sinh(u_b - u_j + 2\eta)}{\sinh(u_b - u_j - 2\eta)} \prod_{j=1\neq a}^{N+1} \sinh(u_b - v_j - 2\eta) + \prod_{j=1\neq a}^{N+1} \sinh(u_b - v_j + 2\eta)\right), \tag{33}$$

for $b < N+1$, and

$$M_{ab} = \frac{1}{\cosh(v_a - \eta)\cosh(v_a + \eta)}, \tag{34}$$

for $b = N+1$. Here, the Bethe equation, Eq. (23), was used to express $a(v_j)/d(v_j)$ in the matrix elements, and some factors in the matrix elements and the overall prefactor cancel out. This result can be checked by a numerical evaluation of the sums over the spacial variables using the coordinate representation in Eq. (3) for a small number of particles $N = 1,2,3$, which we have done.

The determinant results in Eqs. (29), (27), and (32) can be checked by a numerical evaluation of the sums over the spacial variables using the coordinate representation in Eq. (3). However, the latter summation over many coordinates has factorial complexity, which already limits numerical calculations to a few particles on chains of a few dozen sites. The results of the algebraic Bethe ansatz calculations have a power-law complexity that allows general studies, at least numerically, of systems with hundreds of particles on arbitrary long chains without making any approximations, e.g., the studies of correlation functions in one-dimensional systems in Refs. [25–30].

D. The long-wavelength limit

We now turn to the evaluation of the long-wavelength limit for matrix elements in the determinant form with the aim of calculating the determinants explicitly. The resulting expressions will then be used to study physical observables.

Such an analysis is more convenient in the coordinate representation. For small k_j the nonlinear mapping in Eq. (25) becomes linear, similarly to Bethe equation in Eq. (5) in this limit. Then, a simple inversion of the linear function gives

$$u_j = \frac{i}{2}\sqrt{\frac{mU+1}{mU-1}}k_j \quad \text{and} \quad \eta = -\frac{1}{2}\text{acosh}(mU). \tag{35}$$

Note that $|u_j|$ and k_j are simultaneously much smaller than one, while the interaction strength U can be of an arbitrary magnitude.

We start from the expansion of the normalisation factor in Eq. (29) up to the leading nonvanishing order in the quasimomenta. We first substitute Eq. (35) in the matrix elements in Eq. (30), then expand them up to the leading nonvanishing order in $k_j \ll 1$, and obtain the diagonal matrix elements as follows:

$$Q_{aa} = 2\mathcal{L}\sqrt{\frac{mU-1}{mU+1}} - \frac{2(N-1)mU}{\sqrt{m^2U^2-1}} \tag{36}$$

and

$$Q_{ab} = \frac{2mU}{\sqrt{m^2U^2-1}}, \tag{37}$$

for $a \neq b$. The off-diagonal matrix elements are small compared to the diagonal entries as $Q_{ab}/Q_{aa} \sim 1/\mathcal{L}$ so the leading contribution to the determinant is accumulated on the diagonal. Also expanding the prefactor of Eq. (29) in small k_j we obtain the following expression for the normalisation in the long-wavelength limit:

$$\langle \mathbf{k}|\mathbf{k}\rangle = \frac{2^{N^2}(-1)^N(1-mU)^{N^2}\left(\mathcal{L} - \frac{mUN}{mU+1}\right)^N}{i^{N(N-1)}\prod_{i\neq j}(k_j - k_i)}, \tag{38}$$

where k_j are quasimomenta in the coordinate representation of Bethe ansatz.

Our primary interest lies in the spectral function that contains the local matrix element of $\psi_j^\dagger$ operators so here we will focus on the determinant result in Eq. (32). Similarly to the calculation of the normalization factor, we substitute Eq. (35) into Eq. (33), which, however, becomes zero in the zeroth order in k_j. Expanding it up to linear order in k_j we obtain

$$M_{ab} = 2mU(m^2U^2-1)^{\frac{N-1}{2}}\frac{\sum_{j=1}^N k_j^u - \sum_{j=1\neq a}^{N+1} k_j^v}{k_b^u - k_a^v} \tag{39}$$

for $b < N+1$, where $\Delta P = \sum_j k_j^u - \sum_j k_j^v$ is the difference of two conserved quantities, the momenta of two states $\mathbf{k}^u$ and $\mathbf{k}^v$. The matrix elements in Eq. (34) are already nonzero in the zeroth order in k_j giving

$$M_{ab} = \frac{2}{mU+1}, \tag{40}$$

for $b = N+1$. Also expanding the prefactor in Eq. (32) and rearranging the expressions by taking a common factor out of the matrix elements we obtain

$$\left\langle \mathbf{k}^v|\psi^\dagger(0)|\mathbf{k}^u\right\rangle = (-1)^{N+1}i^{N^2}2^{N^2+N+\frac{1}{2}} \times 1 \times \frac{(mU-1)^{N^2+\frac{1}{2}}m^N U^N \mathcal{D}}{\prod_{j<i}^N\left(k_j^u - k_i^u\right)\prod_{j<i}^{N+1}\left(k_j^v - k_i^v\right)}, \tag{41}$$

where the entries of the matrix under the determinant, $\mathcal{D} = \det\hat{\mathcal{M}}$, for $b < N+1$ are

$$\mathcal{M}_{ab} = \frac{\Delta P + k_a^v}{k_b^u - k_a^v} \quad \text{and} \quad \mathcal{M}_{a,N+1} = 1. \tag{42}$$

All matrix elements are of the same order so the determinant in Eq. (41) is a sum of a large number of terms unlike the normalisation factor in Eq. (38). Doing the summation we find an explicit expression in the form of a fraction of two polynomials in quasimomenta of the initial and the final states,

$$\mathcal{D} = (-1)^{N+1}\frac{\prod_j\left(\Delta P + k_j^u\right)}{\prod_{i,j}\left(k_j^v - k_i^u\right)}\prod_{j<i}^{N}\left(k_j^u - k_i^u\right)\prod_{j<i}^{N+1}\left(k_j^v - k_i^v\right). \tag{43}$$

For $N = 1$, the result above is evaluated straightforwardly as a determinant of a 2×2 matrix with the matrix elements in Eq. (42). For arbitrary N we prove it by induction. Using the Laplace development on the $N+1$ row, the determinant

for $N+1$ particles can be expressed as a sum of minors given, in turn, by determinants for N particles, $\mathcal{D}_{N+1} = \sum_{a=1}^{N+2}(-1)^{N+1+a}\mathcal{M}_{a,N+1}\mathrm{minor}_{a,N+1}$, which—let us assume for purposes of the inductive method—are given by Eq. (43):

$$\mathrm{minor}_{a,N+1} = (-1)^{N+1}\frac{\prod_{j=1}^{N}\left(\Delta P + k_j^u\right)}{\prod_{i=1,j=1\neq a}^{N,N+2}\left(k_j^v - k_i^u\right)}\prod_{j<i}^{N}\left(k_j^u - k_i^u\right)\prod_{j<i\neq a}^{N+2}\left(k_j^v - k_i^v\right). \tag{44}$$

Here, $\mathcal{M}_{a,N+1}$ are given by the matrix elements in Eq. (42), N quasimomenta k_j^u are labeled by $j = 1,\ldots,N$, and $N+1$ quasimomenta k_j^v are labeled by $j = 1,\ldots,N+2$ with ath elements excluded. After taking a common factor in front of the sum, the determinant for $N+1$ particles becomes

$$\begin{aligned}\mathcal{D}_{N+1} = (-1)^{N+2}&\frac{\prod_{j=1}^{N+1}\left(\Delta P + k_j^u\right)\prod_{j<i}^{N+1}\left(k_j^u - k_i^u\right)\prod_{j<i}^{N+2}\left(k_j^v - k_i^v\right)}{\prod_{i,j}\left(k_j^v - k_i^u\right)}\\ &\times\frac{1}{\Delta P + k_{N+1}^u}\sum_{a=1}^{N+2}\frac{\left(\Delta P + k_a^v\right)\prod_{j=1\neq a}^{N+2}\left(k_j^v - k_{N+1}^u\right)\prod_{j=1}^{N}\left(k_j^u - k_a^v\right)}{\prod_{j=1}^{N}\left(k_j^u - k_{N+1}^u\right)\prod_{j=1\neq a}^{N+2}\left(k_j^v - k_a^v\right)}.\end{aligned} \tag{45}$$

The sum in the above expression gives, by direct calculation, $\sum_{a=1}^{N+2}\cdots = \Delta P + k_{N+1}^u$, which makes the whole second line unity. The determinant is equal to the first line of Eq. (45), which is also equal to the result in Eq. (43) for $N+1$ particles. Thus we obtained the same result for $N+1$ particles starting from Eq. (43) for N particles. Hence it is proved by induction.

Finally, the form factor in Eq. (9) is the modulus squared of Eq. (41). Normalizing the initial and the final state wave functions using Eq. (38) as $|\langle f|\psi^\dagger(0)|0\rangle|^2 = |\langle\mathbf{k}^f|\psi^\dagger(0)|\mathbf{k}^0\rangle|^2\langle\mathbf{k}^f|\mathbf{k}^f\rangle^{-1}\langle\mathbf{k}^0|\mathbf{k}^0\rangle^{-1}$, we obtain

$$\begin{aligned}|\langle f|\psi^\dagger(0)|0\rangle|^2 = &\frac{Z^{2N}}{\mathcal{L}}\frac{\prod_j^N\left(k_j^0 - P_f\right)^2}{\prod_{i,j}^{N,N+1}\left(k_j^f - k_i^0\right)^2}\\ &\times\prod_{i<j}^{N}\left(k_j^0 - k_i^0\right)^2\prod_{i<j}^{N+1}\left(k_j^f - k_i^f\right)^2,\end{aligned} \tag{46}$$

where $Z = mU/(mU+1)/(\mathcal{L} - NmU/(1+mU))$, k_j^f and k_j^0 are the quasimomenta of the eigenstate $|f\rangle$ and the ground state $|0\rangle$, respectively, and $P_0 = 0$ for the ground state.

The calculation of $\langle f|\rho(0)|0\rangle$ is done in a similar way by expressing the local density operator ρ_1, within the framework of the lattice model, in terms of the algebraic Bethe ansatz operators A, B, C, D and, then, by using the Slavnov formula. Details are given in Appendix B. In the long-wavelength limit, we obtain

$$\begin{aligned}|\langle f|\rho(0)|0\rangle|^2 = &\frac{Z^{2N-2}}{\mathcal{L}^2}\frac{P_f^{2N}}{\prod_{i,j}^{N,N}\left(k_j^f - k_i^0\right)^2}\\ &\times\prod_{i<j}^{N}\left(k_j^0 - k_i^0\right)^2\prod_{i<j}^{N}\left(k_j^f - k_i^f\right)^2,\end{aligned} \tag{47}$$

where the final states $|f\rangle$ have the same number of excitations N as the ground state $|0\rangle$, unlike in Eq. (46), and $P_0 = 0$ for the ground state as in Eq. (46).

These form factors in Eqs. (46) and (47) together with the solution of Bethe equations in Eq. (6) is the main technical result in the theory part of our work. We will analyze its physical consequences in the next two sections. The similarity between these two expressions means that the hierarchy of modes we will identify below is a general feature of one and two body operators.

E. Hierarchy of modes

The results in Eqs. (46) and (47) have one or more singularities when one or more quasimomenta of an excited state coincide with a quasimomentum of the ground state, $k_j^f = k_j^0$. Both results have a multiplicand $Z^{2N} \sim \mathcal{L}^{-2N}$ that becomes virtually zero in the thermodynamic limit, in which $\mathcal{L}\to\infty$. Thus the product of these two opposite factors produces an uncertainty in the limiting behavior (of the $0\times\infty$ type) that has to be resolved. Since we are specifically interested in a transport experiment in this paper, in which the spectral function is measured, we will mainly focus on solving the uncertainty problem for the result in Eq. (46).

The maximum number of singularities is N in the extreme case, when the quasimomenta k_j^f of an excited state coincide with all of the N quasimomenta of the ground state k_j^0 given in Fig. 2(gs). The excited states of this kind are given in Fig. 2(a). The divergences in the denominator of Eq. (46) occur only in the leading order—the first term in Eq. (6)—but the subleading order—the second term in Eq. (6)—already provides a self-consistent cutoff within the theory. The interaction shift of the quasimomenta at subleading order does not cancel for the extra added particle in the excited state, making the factors in the denominator of Eq. (46)

$$k_j^f - k_j^0 = \frac{mU}{mU+1}\frac{k_{N+1}^f - k_j^0}{\mathcal{L} - \frac{mUN}{mU+1}}, \tag{48}$$

where in the right-hand side (r.h.s.), only the first term from Eq. (6) is relevant for k_{N+1}^f and k_j^0. The numerator for the states in Fig. 2(a) becomes

$$k_j^0 - P_f = k_j^0 - k_{N+1}^f. \tag{49}$$

Substitution of Eqs. (48) and (49) in Eq. (46) for one particle, say for $j = N$, cancels one factor $Z^2 \sim \mathcal{L}^{-2}$ and the other part of the product for $i\neq j$ in the denominator of the first line of Eq. (46) cancels partially the products in the second line of Eq. (46). The expression for the remaining $N-1$ particles is the same as Eq. (46) but the numbers of terms in the products

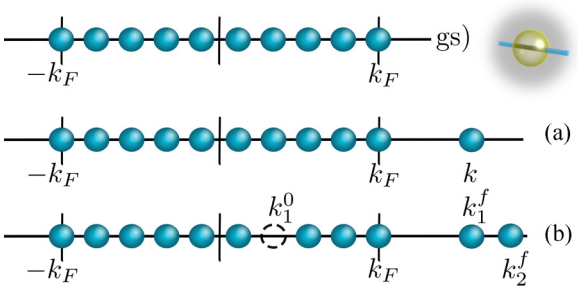

FIG. 2. Configurations of quasimomenta that solve the Bethe equations in Eqs. (5) and (4) for the spinless fermions model in Eq. (2): (gs) the ground state, (a) excitations that form the a level of the hierarchy, and (b) excitations that form the b level of the hierarchy.

are reduced by one, $N \to N-1$, giving

$$|\langle f|\psi^\dagger(0)|0\rangle|^2 = \frac{Z^{2N-2}}{\mathcal{L}} \frac{\prod_j^{N-1}\left(k_j^0 - P_f\right)^2}{\prod_{i,j}^{N-1,N}\left(k_j^f - k_i^0\right)^2} \times \prod_{i<j}^{N-1}\left(k_j^0 - k_i^0\right)^2 \prod_{i<j}^{N}\left(k_j^f - k_i^f\right)^2. \quad (50)$$

Repeating the procedure $N-1$ times, we cancel the remaining Z^{2N-2} factor completely (with the rest of other terms) and obtain

$$\mathcal{L}|\langle f|\psi^\dagger(0)|0\rangle|^2 = 1. \quad (51)$$

Corrections to this result originate from higher subleading orders in the solutions to Bethe equations in Eq. (6) and are of the order of $O(\mathcal{L}^{-1})$. This becomes much smaller than one at the leading order of Eq. (51) in the thermodynamic limit.

Substitution of Eq. (51) in Eq. (9) gives the value of the spectral function $A(k,\varepsilon(k)) = 1$. The energies and the momenta of the excitations in Fig. 2(a) form a single line on the spectral plane, like a single particle with dispersion $\varepsilon(k) = k^2/(2m^*)$, where the effective mass is renormalized by the Luttinger parameter K, $m^* = mK$ [47]. Note that, since we still resolve individual levels here, the delta functions in the definition of the spectral function in Eq. (9) become discrete Kronecker deltas. Thus $A(k,\varepsilon)$ at each discrete point k,ε describes the probability of adding (removing) a particle, which is non-negative and is bound by one from above, instead of the probability density as in the continuum case. Dimensional analysis makes this distinction clear immediately.

The excitations that have one singularity less ($N-1$ in total) can be visualized systematically as an extra electron-hole pair created in addition to adding an extra particle, see Fig. 2(b). Staring from Eq. (46) and using the same procedure as before Eq. (50) but $N-1$ instead of N times, we obtain

$$|\langle f|\psi^\dagger(0)|0\rangle|^2 = \frac{Z^2}{\mathcal{L}} \frac{\left(k_2^f - k_1^f\right)^2\left(k_1^0 - P_f\right)^2}{\left(k_1^f - k_1^0\right)^2\left(k_2^f - k_1^0\right)^2}, \quad (52)$$

where k_1^f, k_2^f, and k_1^0 are positions of two particles and one hole in Fig. 2(b). Substitution of Eq. (52) in Eq. (9) gives values of the spectral function $A(k,\varepsilon) \sim \mathcal{L}^{-2}$ that are smaller than the values for the excitations in Fig. 2(a) [in Eq. (9)] by a factor of $\mathcal{L}^{-2}$. For two singularities less ($N-2$ in total), we find $A(k,\varepsilon) \sim \mathcal{L}^{-4}$ and so on.

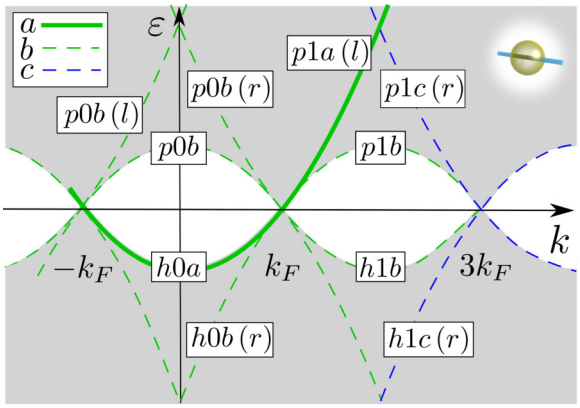

FIG. 3. The spectral function for interacting spinless fermions in the region $-k_F < k < k_F$ ($k_F < k < 3k_F$) labeled by 0(1). The grey areas mark nonzero values. The green and the blue lines are modes of the hierarchy labeled as follows: $p(h)$ shows the particle (hole) sector, k_F is the Fermi momentum, a, b, c, respectively, identify the level in the hierarchy in powers 0, 1, 2 of $\mathcal{R}^2/L^2$, and (r,l) specifies the origin in the range—modes on the edge have no such label.

This emerging structure separates the plethora of many-body excitations into a hierarchy according to the remaining powers of $\mathcal{L}^{-2}$ in their respective form factors. We label the levels of the hierarchy as a, b, c reflecting the factors $\mathcal{L}^{-2n}$ with $n = 0, 1, 2$. While the leading a excitations form a discrete single-particle-like dispersion, see $h0a$ and $p1a(l)$ lines in Fig. 3, the spectral properties of the subleading excitations are described by a more complicated continuum of states on the energy-momentum plane. We will explore the b excitations below.

All simple modes, formed by single-particle and holelike excitations of the type in Fig. 2(b), in the range $-k_F < k < 3k_F$ are presented in Fig. 3. We use the following naming scheme: $p(h)$ indicates the particle (hole) sector, 0(1) encodes the range of momenta $-k_F < k < k_F (k_F < k < 3k_F)$, a, b, c reflect the terms $\mathcal{L}^{-2n}$ with $n = 0, 1, 2$. The suffix (r) or (r) marks a particlelike mode, e.g., the states with in Fig. 2(b) with $k_1^f = -k_F - \gamma$, $k_1^0 = k_F$, and $k_F > P_f = -2k_F + k_2^f > -k_F$ forms the mode $p0b(l)$. Holelike modes have no suffixes, e.g., the states in Fig. 2(b) with $k_1^f = -k_F - \gamma$, $k_2^f = k_F + \gamma$, and $-k_F < P_f = -k_1^0 < k_F$ form the mode $p0b$. Simple modes formed by excitations of lower levels of the hierarchy are obtained by translation of the b modes constructed in this paragraph by integer numbers of $\pm 2k_F$. A couple of simple modes formed by c excitations are presented on Fig. 3. They have the same naming scheme as the b modes.

Now we evaluate values of the spectral function along all simple b modes in the range $-k_F < k < 3k_F$. Let us start from the $p0b$ mode, see Fig. 3. Along this mode, the spectral function is a bijective function of k, $A(k,\varepsilon_{p0b}(k))$ where $\varepsilon_{p0b}(k) = k_F^2/(mK) - k^2/(2mK)$. The states that form it belong to b excitations in Fig. 2(b) with $k_1^f = -k_F - \gamma, k_2^f = k_F + \gamma$, and $k = P_f = -k_1^0$. Substituting this parametrization

TABLE I. Spectral weights along the a and the b modes for $-k_F < k < k_F$ ($k_F < k < 3k_F$) labeled by $x = 0(1)$. Terminology is the same as in Fig. 3; $\gamma = 2\pi/\mathcal{L}$ and $Z = mU/(mU+1)/(\mathcal{L} - NmU/(1+mU))$.

	$x=0$	$x=1$
pxa		1
hxa	1	
pxb	$\frac{16Z^2k_F^2k^2}{(k^2-(k_F+\gamma)^2)^2}$	$\frac{4Z^2\gamma^2(k-k_F+\frac{3}{2}\gamma)^2}{(k-k_F+\gamma)^2(k-k_F+2\gamma)^2}$
$pxb(l)$	$\frac{4Z^2(k_F+k)^2}{k_F^2}$	
$pxb(r)$	$\frac{4Z^2(k_F-k)^2}{k_F^2}$	
hxb		$\frac{4Z^2(3k_F-k-\gamma)^2(k_F+k)^2}{k_F^2(k-k_F+\gamma)^2}$
$hxb(l)$	$\frac{4Z^2\gamma^2}{(k+k_F+2\gamma)^2}$	$\frac{Z^2k_F^2k^2}{((k+\gamma)^2-k_F^2)^2}$
$hxb(r)$	$\frac{4Z^2\gamma^2}{(k-k_F-2\gamma)^2}$	

in Eq. (52), we obtain

$$A(k,\varepsilon_{p0b}(k)) = \frac{16Z^2k_F^2k^2}{(k^2-(k_F+\gamma)^2)^2}. \tag{53}$$

The spectral function along all other b modes in Fig. 3 is calculated in the very same way and the results (together with a modes) are summarized in Table I.

The amplitude of the subleading b excitations does not vanish in the thermodynamic limit, though it is proportional to $1/\mathcal{L}$. The limit involves both $\mathcal{L}\to\infty$ and the particle number $N\to\infty$ but keeps the density $N/\mathcal{L}$ finite. The spectral weights of the subleading modes $p0b$, $h1b$, and $h1b(r)$ from Table I are proportional to the density squared for some values for k, e.g., the modes $p0b$ at $k = k_F$ gives

$$A(k_F,\varepsilon_{p0b}(k_F)) = \left(\frac{mU}{1+mU}\right)^2 \frac{N^2}{\left(\mathcal{L}-\frac{NmU}{1+mU}\right)^2}, \tag{54}$$

see Table I for other modes, and are apparent in the infinite system.

Assessing further the continuum of b excitations we consider the spectral function and how it evolves as one moves away slightly from the of the strongest a mode. Just a single step of a single quantum of energy away from the a mode requires the addition of an electron-hole pair on top of the configuration of quasimomenta in Fig. 2(a). This immediately moves such states one step down the hierarchy to b excitations. Let us consider the spectral function as a function of energy only making a cut along a line of constant k. The energies of the electron-hole pairs themselves are regularly spaced around the Fermi energy with slope v_F. However, the degeneracy of the many-body excitations due to the spectral linearity makes the level spacings nonequidistant. We smooth this irregularity using an averaging of the spectral function over energy,

$$\overline{A}(k,\varepsilon) = \int_{-\frac{\epsilon_0}{2}}^{\frac{\epsilon_0}{2}} \frac{d\epsilon}{\epsilon_0} A(k,\varepsilon+\epsilon), \tag{55}$$

where ϵ_0 is a small energy scale.

Then, using the parametrization of b excitations in Fig. 2(b) in the vicinity of the principal parabola, we linearize the energies of the extra electron-hole pairs around the Fermi energy and of the particle around its original position. We then substitute the resulting expressions for $k_{1,2}^f$ and k_1^0 in terms of the energy E from Eq. (7) in Eq. (52), similar to our procedure of obtaining Eq. (53). Finally, we use the averaging rule in Eq. (55) and obtain

$$\overline{A}(k,\varepsilon) = \frac{Z^2 2k_F\left(3k^2+k_F^2\right)\theta(\varepsilon_{h0a}(k)-\varepsilon)}{m\gamma K(\varepsilon_{h0a}(k)-\varepsilon)} \quad \text{for } -k_F < k < k_F, \tag{56}$$

$$\overline{A}(k,\varepsilon) = \frac{Z^2[k+\mathrm{sgn}(\varepsilon-\varepsilon_{p1a(l)}(k))k_F]^3}{m\gamma K|\varepsilon-\varepsilon_{p1a(l)}(k)|} \quad \text{for } k_F < k < 3k_F, \tag{57}$$

where $\gamma = 2\pi/\mathcal{L}$ and $\varepsilon_{h0a}(k) = \varepsilon_{p1a(l)}(k) = k^2/(2mK)$ is the parabolic dispersion of the a mode.

The result in Eqs. (56) and (57) can be interpreted as the line shape of the a mode. However, it has an unusual form—namely that of a divergent power law. The divergence at the parabola is cut off by the lattice spacing recovering $\overline{A}(k,\varepsilon_{h0a,p1a}(k)) = 1$ from Eq. (51). In Eq. (57), the line shape is asymmetric due to different prefactors $(k\pm k_F)^3$ above and below the line. In Eq. (56), the higher energy part $[\varepsilon > \varepsilon_{h0a}(k)]$ is absent due to the absence of the excitation in this region, forbidden by the kinematic constraint.

Not every simple mode marks a distinct feature. The states at least on one side, above or below the mode in energy, have to belong to a different level of the hierarchy than the mode itself, which results in a divergence or in a jump of the spectral function in the continuum of excitations. Otherwise, the spectral function is continuous across all of the modes that belong to the same level of the hierarchy as the excitations around them. The a modes are distinct since excitations around them belong to a different b level. All modes on the spectral edges, $p0b$, $p1b$, $h1b$, and so on, are distinct since on one side there are no excitations (due to the kinematic constraint) and on the other side there is a finite density of states resulting in a jump of the spectral function.

An example of an observable subleading mode in the continuum is $h0b(r)$. On the higher-energy side of this mode, the excitations are described by the same type of states in Fig. 2(b) but on the lower-energy side creation of an additional electron-hole pair in the quasimomenta results in states that have two noncancelled singularities in Eq. (46), which lowers their corresponding level of the hierarchy to c from b. This, in turn, results in an observable feature in the spectral function

at the position of the $h0b(r)$ mode. On the other hand, the $p0b(r)$ and $h1b(l)$ modes in continuum are not detectable since excitations on both sides around them belong to the same b level of the hierarchy. Observability of all other modes can be easily assessed in the same way by considering their corresponding states in the form of Figs. 2(a) and 2(b) and excitations around the modes.

The structure of the matrix element in Eq. (47) is quite similar to the matrix element in Eq. (46). Thus the dynamical structure factor exhibits the same hierarchy of excitations (and modes formed by them) as the spectral function analysed in detail in this section. The strongest excitations correspond to only a single electron-hole pair, the first subleading level corresponds to two electron-hole pairs, and so on.

Also, a similar hierarchy of excitations was observed in numerical studies of spin chains, e.g., Refs. [25–27,31–33]. There, it was found that only a small number of electron-hole pairs are sufficient to saturate the sum rules for the dynamics response functions. For example, integration of Eq. (9) over the energy and momentum,

$$\int d\varepsilon dk A(k,\varepsilon) = \mathcal{L} - N, \tag{58}$$

gives the number of empty sites. If a sum over only a small number of electron-hole pairs in the intermediate state f in Eq. (9) is sufficient to fulfill this rule in Eq. (58) then a few electron-hole pairs already account for a major part of all of the spectral density and the states with more electron-hole pair have vanishing spectral weights, as in the hierarchy of modes established in this work. Our analytic work demonstrates how this can arise in a Bethe ansatz solution, though the numerical studies of spin chains were done at large fillings ($\mathcal{L} \sim N$), for which our result in Eq. (46) is not directly applicable.

F. Spectral edge modes

In this section, we consider another important role played by the continuum of eigenstates, namely how they form the spectral function close to the spectral edges. These edges separate regions where there are excitations from regions where there are none, see borders between white and grey regions in Fig. 3. The recently proposed model of a mobile impurity [34–37] gives a field-theoretical description of the dynamic response functions around the spectral edges predicting a general (divergent) power-law behavior $A(k,\varepsilon) \sim |\varepsilon - \varepsilon_{\text{edge}}(k)|^{-\alpha}$, see Refs. [28,34–37,40–46]. For spinless fermions, the exponent of the spectral function is given by [47]

$$\alpha = 1 - \frac{K}{2}\left(1 - \frac{1}{K^2}\right) \tag{59}$$

for both the particle ($p0b$) and hole edges ($h0a$), where Eq. (8) gives the Luttinger parameter K in terms of the microscopic parameter of the model in Eq. (1). Here, we will compare the field-theoretical result in Eq. (59) with the microscopic calculation in Eqs. (6) and (46). We find agreement in many cases, but interestingly we also find some cases where the mobile impurity results are not consistent with the analytic solution, suggesting this field-theoretical approach is not the complete story.

The hole edge is an a mode, $h0a$, whereas the continuum around it is dominated by b excitations. The spectral function formed by these b excitations has already been calculated in Eq. (56) giving the power-law behavior with the exponent $\alpha = 1$. Note that for spinless fermions the Luttinger parameter K has only small deviations from 1 for arbitrary magnitude of the short-range interactions, see Eq. (8). This makes the result in Eq. (59) close to $\alpha = 1$ for all values of U; comparison of small deviations (which are U-dependent) require a better accuracy in evaluating Eq. (56). Thus the result of the microscopic calculation coincides with the prediction of the mobile-impurity model in Eq. (59) for the hole edge.

The particle edge is a b mode, $p0b$, and the excitations around it belong to the same b level of the hierarchy as the mode itself. Parameterizing the b excitations in this region of the continuum as in Fig. 2(b) and using the averaging procedure in Eq. (55) we obtain, repeating the same steps as before, Eqs. (56) and (57),

$$\overline{A}(\varepsilon) \sim (\varepsilon - \varepsilon_{p0b})^3 \tag{60}$$

for $k \approx 0$ to

$$\overline{A}(\varepsilon) \sim \text{const} - (\varepsilon - \varepsilon_{p0b}) \tag{61}$$

for $k \approx k_{\text{F}}$, where $\varepsilon_{p0b}(k) = k_{\text{F}}^2/(mK) - k^2/(2mK)$. This is a new power-law behavior characterized by an exponent α changing essentially with k from $\alpha = -3$ for $k = 0$ to $\alpha = -1$ for $k \approx \pm k_{\text{F}}$ and is *different* from the predictions of the mobile-impurity model in Eq. (59). Here, we observe that the phenomenological model in Refs. [34–36] is correct only for the a-mode spectral edge but higher-order edges would require a different field-theoretical description.

On a more detailed level, the difference between the particle and the hole edges manifests itself in different statistics of level spacings around the edges. An evaluation of the density of states, $\nu(k,\varepsilon) = \sum_f \delta(\varepsilon - E_f)\delta(k - P_f)$, is performed using E_f from Eq. (7) for a fixed momentum k. For b excitations in Fig. 2(b), we obtain the same results,

$$\nu(k,\varepsilon) \sim |\varepsilon - \varepsilon_{p0b(h0a)}(k)|, \tag{62}$$

in the vicinity of both the particle $p0b$ and the hole $h0a$ edges. However, the statistics of the level spacings

$$\mathcal{P}(s,k) = \sum_f \delta(s - (E_{f+1} - E_f))\delta(k - P_f), \tag{63}$$

where E_f are assumed sorted by their values, is different in the two regions. For the hole edge, the energy levels are spaced regularly and are governed by the slope of dispersion at the Fermi energy $\approx v$. This gives a bimodal $\mathcal{P}(s,k)$ with a sharp peak at $s = 0$ (due to many-body degeneracy of almost linear spectrum at E_{F}) and at $s \approx v\gamma$. For the particle edge, the statistics of the level spacings varies from having a regular level spacing [for k commensurate with k_{F} in Fig. 4(a)] to an irregular distribution [for incommensurate k in Fig. 4(b)].

The change in the characteristics of the underlying statistics is another microscopic difference between the particle (b-mode) and the hole (a-mode) edges that signals a difference in underlying physics for the particles and for the holes spectral edges beyond the low-energy region.

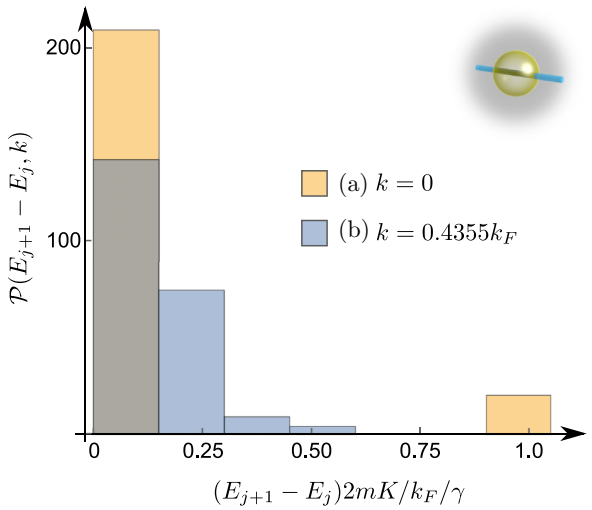

FIG. 4. Distributions of level spacings in the vicinity $(\max(E_f-\varepsilon_{p0b}(k))/\varepsilon_F = 1/100)$ of the particle mode $p0b$ accumulated along energy axis for the values of momenta (a) $k=0$ and (b) $k=0.4355k_F$; $N=2\times10^3$ and $L=2\times10^5$.

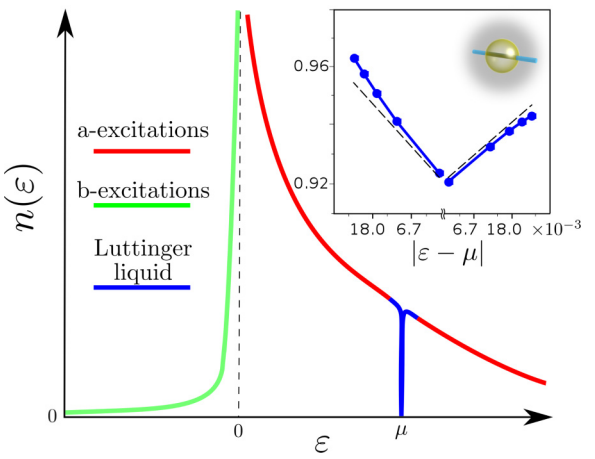

FIG. 5. The local density of states for interacting spinless fermions: the red and the green lines show the contribution of a and b excitations and the blue line indicates the Luttinger-liquid regime. Inset is a log-log plot around the Fermi energy: the points are numerical data for $N=71$, $L=700$, $mV=6$ giving $K=0.843$, and the dashed line is $n(\varepsilon)=\text{const}|\varepsilon-\mu|^{(K+K^{-1})/2-1}$.

V. LOCAL DENSITY OF STATES

Now we turn to another macroscopic observable, the local density of states (LDOS), which describes the probability of tunneling a particle in or out of the wire at a given position in space and at a given energy. Since the model in Eq. (1) is translationally invariant, the LDOS depends only on a single variable—energy, making it a more convenient quantity to study qualitatively how the physical properties change from low to high energies. In this section, we will show how the power-law result of the Tomonaga-Luttinger model [2] at low-energy crosses over into the hierarchy of mode-dominated behavior at high energy.

The probability of local tunneling at energy ε and at position x is described by [16] $n(x,\varepsilon) = -\text{Im}[\int dt e^{-i\varepsilon t}G(x,x,t)]\text{sgn}(\varepsilon-\mu)/\pi$, where μ is the chemical potential and $G(x,x',t) = -i\langle T(e^{-iHt}\psi(x)e^{iHt}\psi^\dagger(x'))\rangle$ is the two-point correlation function at zero temperature. In terms of eigenmodes, it reads

$$n(\varepsilon) = \mathcal{L}\sum_f [|\langle f|\psi^\dagger(0)|0\rangle|^2\delta(\varepsilon - E_f + E_0) + |\langle 0|\psi(0)|f\rangle|^2\delta(\varepsilon + E_f - E_0)], \quad (64)$$

where the coordinate dependence drops out explicitly, the eigenenergy E_f has already been calculated in Eq. (7) and the matrix elements $|\langle 0|\psi(0)|f\rangle|^2$ are given in Eq. (46). Note that the definition in Eq. (64) is connected to the definition of the spectral function in Eq. (9) via

$$n(\varepsilon) = \int dk A(k,\varepsilon). \quad (65)$$

The leading contribution for $\varepsilon > 0$ comes from a excitations. Substituting the matrix element for the a excitations from Eq. (51), we sum over the single-particle-like excitations [with $\varepsilon = k^2/(2mK)$] that form the mode and obtain

$$n(\varepsilon) = \sqrt{\frac{2mK}{\varepsilon}}\theta(\varepsilon). \quad (66)$$

This result gives the same $1/\sqrt{\varepsilon}$ functional dependence—see red line in Fig. 5—and the same $1/\sqrt{\varepsilon}$ van Hove singularity at the bottom of the band $\varepsilon = 0$ as the free-particle model.

For $\varepsilon < 0$, the leading contribution to $n(\varepsilon)$ comes from b excitations. Instead of performing a summation in Eq. (64) over every b excitation in this region, we use an intermediate result in Eq. (56) where the matrix elements of b excitations in Eq. (52) are already smoothed over many eigenstates and the relation in Eq. (65). Evaluating the integral over k in Eq. (65), after the substitution of Eq. (52) into it, for $\varepsilon < 0$ we obtain

$$n(\varepsilon) = \frac{2Z^2k_F^2}{\gamma\mu K}\theta(-\varepsilon) \times\left[2\left(1-\frac{3|\varepsilon|}{\mu}\right)\sqrt{\frac{\mu}{|\varepsilon|}}\cot^{-1}\left(\sqrt{\frac{|\varepsilon|}{\mu}}\right)+6\right]. \quad (67)$$

There is a finite probability to find a particle below the bottom of the conduction band—green line in Fig. 5—which is allowed only due to interactions between many particles. The factor Z is proportional to the interaction strength V—see Eq. (46)—making $n(\varepsilon)=0$ for $\varepsilon<0$ in the free particle limit of $V=0$. At the bottom of the band below the $\varepsilon=0$ point in Fig. 5, the result in Eq. (67) contains another Van Hove singularity,

$$\rho(\varepsilon) = \frac{2\pi Z^2k_F^2}{\gamma K\sqrt{\mu|\varepsilon|}}, \quad (68)$$

which also disappears when $V=0$. The appearance of the identical exponent as in Eq. (66) exponent $1/\sqrt{|\varepsilon|}$ seems coincidental.

Around the Fermi energy (the point $\varepsilon=\mu$ in Fig. 5), the Tomonaga-Luttinger model predicts a power-law suppression

of LDOS,

$$n(\varepsilon) \sim |\varepsilon - \mu|^{(K+K^{-1})/2-1}, \tag{69}$$

e.g., see the book in Ref. [2]. However, the result for the a-mode in Eq. (66) is finite at this point, $n(\mu) = \sqrt{2mK/\mu}$. In order to resolve the apparent discrepancy, we evaluate $n(\varepsilon)$ numerically around the Fermi energy using the determinant representation of the form factors in Eqs. (32) and (33) instead of Eq. (46), which accounts for all orders in $1/\mathcal{L}$, and indeed find a suppression of LDOS around $\varepsilon = \mu$, see blue line in the inset in Fig. 5. This signals that the leading-order expansion in the $\mathcal{L}|\langle f|\psi^\dagger(0)|0\rangle|^2 = 1$ result is insufficient at low energies. Very close to the Fermi point (the linear region of the single-particle dispersion) all $1/\mathcal{L}$ orders of the Bethe ansatz calculation are needed to reproduce the result of the Tomonaga-Luttinger model, see dashed lines in the inset in Fig. 5. However, away from the linear region, the particle-hole symmetry of the Tomonaga-Luttinger model is broken by the finite curvature of the dispersion and only the leading $1/\mathcal{L}$ order in Eq. (46) is sufficient to account for the main contribution there.

The general picture emerging in Fig. 5 is a power-law crossover between different energy scales. At low energies (blue region in Fig. 5) Eq. (46) breaks down and the collective modes of the Tomonaga-Luttinger model are a better description of the system. At high energies (the red and the green regions in Fig. 5), the hierarchy of modes, which directly follows from Eqs. (46) and (6), becomes the dominant physical picture. For spinless fermions, the extent of the crossover region is large due to only small deviations from $K = 1$ for arbitrary short-range interactions. For very small exponents $[(K + K^{-1})/2 - 1] \ll 1$, the power-law in Eq. (69) deviates significantly from 1 only in an extremely narrow region around $\varepsilon = \mu$ having a large window of energies where it overlaps with the a-mode result in Eq. (66).

VI. EXPERIMENTS ON SPINFUL FERMIONS

So far, in this paper, we have established the theoretical framework for expecting a hierarchy of modes in a interacting system at high energy. Now we turn to a measurement of tunneling of electrons in a one-dimensional (1D) nanostructure, which gives experimental evidence for the existence of the hierarchy. Electrons have spin 1/2, which does not correspond directly to the model of spinless fermions in Eq. (1), and there is currently no known method for calculating the necessary form factors for spinful fermions. However, the general picture that emerges from the experiment is qualitatively the same as our result in the theory part of this paper.

The design of our device [12] is based on a high-mobility GaAs–AlGaAs double-quantum-well structure (blue and yellow layers in Fig. 6), with electron densities around 3 and 2×10^{15} m^{-2} in the upper and lower layers, respectively, before application of gate voltages. Electrons in the upper layer are confined to a 1D geometry ("wires") in the x direction by applying a negative voltage to split "finger" gates on the surface (gold layer in Fig. 6).

Electrons underneath the gates are completely depleted, but electrons below the gap between gates are squeezed into a narrow 1D wire. The extremely regular wires are arranged

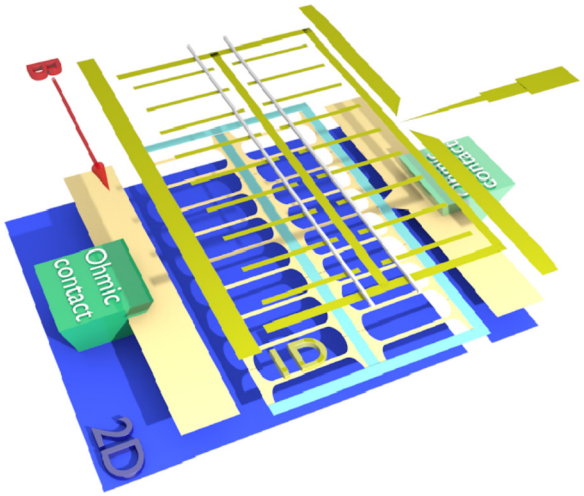

FIG. 6. Schematic of the device made out of a double-well heterostructure. The dark blue and cream layers are the lower and upper quantum wells, respectively. The lower layer hosts the two-dimensional electron gas (2DEG). The wires are defined in the upper layer by gating. The gold top layer represents metallic gates deposited on the surface of the semiconductor heterostructure. The array of parallel "finger" gates defines the 1D wires in the upper well. The white lines represent air bridges joining the finger gates together. Current is injected from the ohmic contact on the right solely into the upper well through the constriction at top right in the diagram. The constriction is formed and pinched off by a split pair of gates, and charge is induced again in the upper well in the constriction by a gate in the center of the channel. The current then flows into the 1D wires via the narrow, nominally 2D, regions shown in light blue. Tunneling to the 2DEG below is possible, and this gives a small "parasitic" current in parallel with the tunnel current from the 1D wires. To tune this tunneling off resonance in the regions of interest by changing the density, a "p" gate is placed above the "p"' regions and a voltage V_P is applied. Current is prevented from flowing from the upper well into the left-hand ohmic contact by a barrier gate shown on the left, which only depletes the upper well. The red arrow shows the direction of the externally applied magnetic field B, which is in the plane of the wells and perpendicular to the wires.

in an array containing ∼600 of them to boost the signal. The small lithographic width of the wires, ∼0.18 μm, provides a large energy spacing between the first and second 1D subbands defined by spatial modes perpendicular to the wires (∼3−5 meV, probably somewhat smaller than for overgrown wires [11]). This allows a wide energy window for electronic excitations in the single 1D subband that covers a range of a few chemical potentials of the 1D system. The lower 2DEG (blue in Fig. 6) is separated from the wires by a $d = 14$ nm tunnel barrier. The wafer is doped with Si symmetrically in the AlGaAs barriers above and below the pair of wells. The doping is separated from the wells by spacer layers. The spacing between the centres of the two quantum wells is nominally $d = 32$ nm but we find a value of $d = 35$ nm fits the data better, and this can be explained by the fact that the centres of the wave functions will be slightly further apart owing to the opposite electric fields in each well.

The 2DEG in the lower (dark blue) layer is used as a controllable injector or collector of electrons for the 1D

system [48,49]. The current I tunneling in the z direction between the layers is proportional to the convolution of the 1D and 2D spectral functions (a pair of peaks at $k_x = \pm k_F$ broadened in k_y by the 1D confinement, and a circle, respectively). An in-plane magnetic field B applied in the y direction, perpendicular to the wires (show with a red arrow in Fig. 6), produces a Lorentz force that changes the longitudinal momentum k_x acquired while tunneling between layers by $\Delta k = eBd/\hbar$, where e is the electronic charge. Thus B shifts the spectral functions in k_x relative to each other, and so probes the momentum. One spectral function can also be shifted relative to the other in energy by applying a voltage V between the layers, in order to probe the 1D and 2D dispersion relations at different energies. The conductance $G = dI/dV$ has a peak when the sharp features in the spectral functions have a significant overlap. At $V = 0$, this occurs when Δk is equal to the sum or difference of the Fermi wave numbers k_F and k_2 of the 1D and 2D systems, respectively, so there are two peaks for $B > 0$, at $B_\pm = \frac{\hbar}{ed}|k_2 \pm k_F|$. By sweeping B and V, one can map out the dispersion relation of states in each layer. The range of magnetic fields that we apply to the system is still within the regime of Pauli paramagnetism for the electron densities in our samples.

VII. LOW ENERGY

The results from two samples are presented, each consisting of a set of identical wires of length $L = 10\,\mu$m (sample A) and $L = 18\,\mu$m (sample B). First, we measure the tunneling conductance $G = dI/dB$ in a small range of voltages and magnetic fields around $V = 0$ and $B = B_+ = 3.15$ T that corresponds to a region on the momentum-energy plane around the Fermi point ($\varepsilon = \mu, k = k_F$), see Fig. 7. Below the Fermi energy, we observe splitting of the single-particle line into two lines with different dispersions—spin (S) and charge (C) separation [11,12]—giving two different slopes v_s and v_c (black dashed lines in Fig. 7). We assume that v_s is the same as for noninteracting electrons and so take it to be the gradient

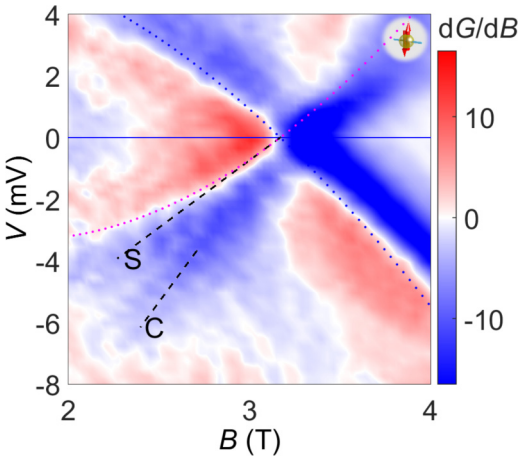

FIG. 7. Intensity plot of dG/dB at low energies around the Fermi point k_F. Spin (S) and charge (C) dispersions are indicated by dashed lines. The dotted lines indicate the parabolae expected in the noninteracting model. The finger-gate voltage $V_F = -0.70$ V and the temperature $T \sim 300$ mK (sample A).

of the parabola at $V = 0$. We estimate v_c from the positions of steepest gradient and hence obtain $v_s \approx 1.2 \times 10^5$ ms^{-1} and $v_c \approx 2.3 \times 10^5$ ms^{-1} at the finger-gate voltage $V_F = -0.70$ V.

Theoretically, the low-energy physics of the interacting 1D electrons is described well by a spinful generalization of the Luttinger-liquid model [2]. Its excitations are collective hydrodynamiclike modes that are split into charge-only and spin-only excitations. For any finite strength of the interactions between fermions, the two types of modes have linear dispersions with different slopes v_c and v_s. In the absence of interactions, the difference between the two velocities vanishes in accordance with the free-electron model, in which the spin degree of freedom does not affect the spectrum but results only in the double degeneracy of the fermionic states. Thus the ratio of v_c/v_s serves as a good measure of the interaction strength. Since the Coulomb interaction between electrons is repulsive, the charge branch always has a steeper slope $v_c \geqslant v_s$ (see Ref. [2]). Thus the ratio varies from 1 for free to ∞ for infinitely repelling particles. In our experiment, we measure the tunneling of electrons and observe two peaks that we attribute to the charge and the spin dispersions. The pair of velocities above gives a large $v_c/v_s \approx 1.8 \pm 0.1$ (for $V_F = -0.70$ V), confirming that our system is in the strongly interacting regime.

VIII. HIGH ENERGY

Now we extend the ranges of the voltage and magnetic field measuring the tunneling conductance G across the double quantum well in Fig. 6 accessing a large portion of the 1D spectral function from below $-k_F$ to $3k_F$ and from -2μ to 2μ, see Fig. 8. There is an unavoidable "parasitic" ("p") tunneling from narrow 2D regions (light blue strips in Fig. 6) that connect the wires to the injector constriction. This superimposes a set of parabolic 2D-2D dispersions on top of the 1D-2D signal, which are marked by magenta and blue dotted lines in Fig. 8.

Apart from the parasitic and the 2D dispersion signals, we observe only a single 1D parabola away from $B = 0$, marked by the solid green line in Fig. 8. It extends from the spin-excitation branch at low energy and the position of its minimum multiplied by the electronic charge e gives the 1D chemical potential $\mu \approx 4$ meV. The B_- and B_+ crossings with the line $V = 0$, corresponding to momenta $-k_F$ and k_F, give the 1D Fermi momentum $k_F \approx 8 \times 10^7$ m^{-1}. All other edges of the 1D spectral function are constructed by mirroring and translation of the hole part of the observable 1D dispersion, dashed green and blue lines in Fig. 8.

For positive voltages in the region just above the higher $V = 0$ crossing point (B_+, which corresponds to k_F), we observe a distinctive feature: the 1D peak broadens, instead of just continuing along the noninteracting parabola, with one boundary following the parabola $[p1a(l)]$ and the other bending around, analogous to the replica $p1b$. This is visible in the conductance, but is most easily seen in the differentials, particularly dG/dV (left column of Fig. 8). The broadening is observed at temperatures from 100 mK up to at least 1.5 K, and in samples with different wire designs (with or without air bridges) and lengths: in Fig. 9, dG/dV is shown in detail for the broadened "replica" region for the 10-μm wires already presented (a)–(d), and for another sample with wires 18-μm long [(e) and (f)]. G is plotted in Figs. 9(b) and 9(d) and f

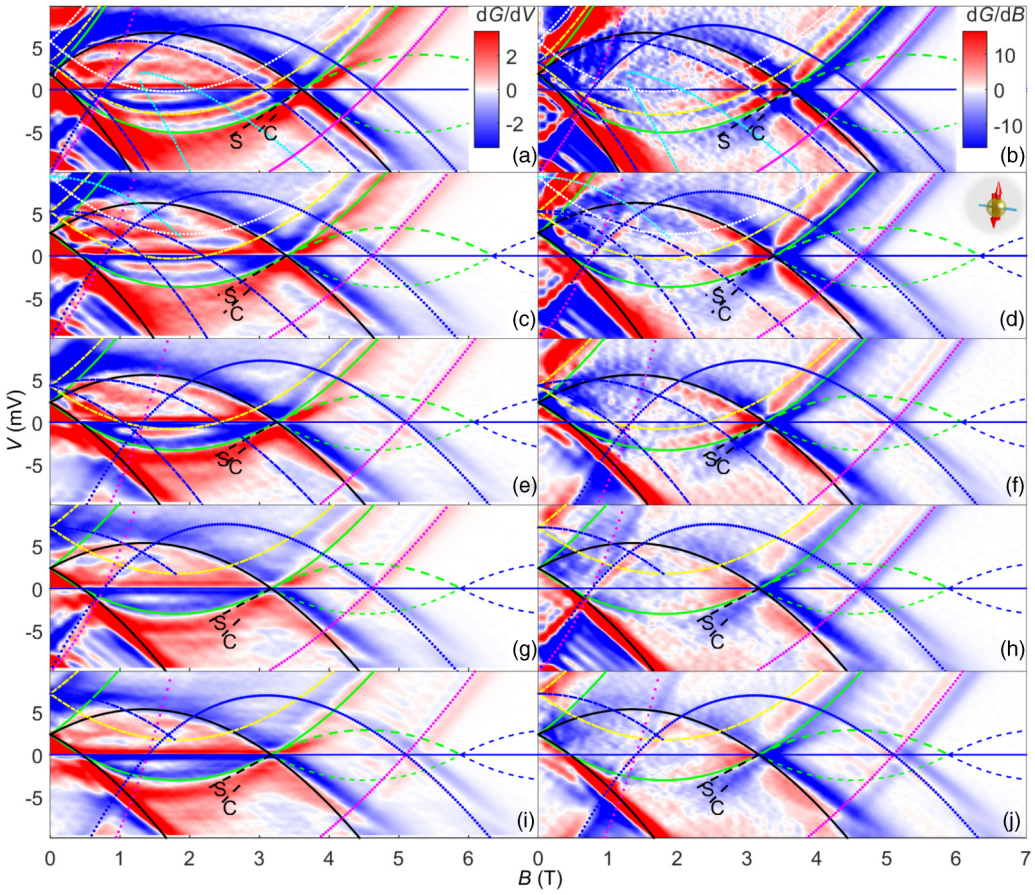

FIG. 8. Intensity plots of dG/dV (left column, in μS/mV) and dG/dB (right column, in μS/T) from below $-k_F$ to above $3k_F$ and from $\sim -2\mu$ to $\sim\mu$, for various finger-gate voltages: -0.60 [(a) and (b)], -0.65 [(c) and (d)], -0.68 [(e) and (f)], and -0.70 V [(g)–(j)]. The solid black lines map out the dispersion of the lower (2D) layer. The green solid line marks a modes, thick and thin dashed green lines, $p1b$ and $h1b$ modes, respectively, and dashed blue, higher-k modes (as in Fig. 3). Dot-dashed yellow (blue) and dotted white (cyan) lines show second and third 1D subbands (2D dispersion measured by those subbands), respectively (though the third is empty, electrons can tunnel into it from the 2D layer and hence there are sometimes signs of its effects for $V > 0$, especially near $B = 0$). Dotted magenta and blue lines are "parasitic" 2D dispersions of the two layers. The voltage on the gate over this region $V_P = 0$ V except for [(e) and (f)] ($V_P = 0.2$ V) and [(i) and (j)] ($V_P = 0.3$ V), which shifts the parabolae to the right without changing the signal from the 1D wires. The lines have all been adjusted to take account of the capacitive coupling between the layers. Spin (S) and charge (C) modes are indicated with black dashed lines. $T \sim 300$ mK. See Table II for the densities and the ratio v_c/v_s for each gate voltage.

on cuts along the V axis of the corresponding plots in the left column at various fields B from B_+ to 4.8 T—between the "+" and "×" symbols on each curve is a region of enhanced conductance characteristic of the replica $p1b$.

Filling of the second 1D subband changes significantly the screening radius for the Coulomb interaction potential in the first 1D subband. This is manifested by a change of the ratio v_c/v_s when the occupation of the second subband is changed by varying voltage of the finger gates V_F in Figs. 8(a), 8(c), 8(e), and 8(g), see Table II. The ratio v_c/v_s is a measure of interaction energy. Thus the finger gates give a degree of experimental control over the interactions within our design of the 1D system. We use the maximum change of the ratio v_c/v_s for different finger gate voltages to estimate the relative change of the interaction strength as $(\max(v_c/v_s) - \min(v_c/v_s))/\min(v_c/v_s)$ obtaining a change of about 20%.

It also has to be noted that the "replica" is visible even when a second subband is present in the 1D wires, see Figs. 8(a)–8(f). In (a) and (b), it appears to go 25%–30% higher in voltage than expected for a precise copy of the usual 1D parabola (even allowing for capacitive correction) due to a contribution of the second subband, which we do not analyze in detail here.

At even higher magnetic fields, the $p1b$ line passes a "p" parabola. Figures 9(a) and 9(c) [and the corresponding cuts (b) and (d)] show the replica feature for two different positions of

TABLE II. Densities of the 2D layer (n_{2D}) and of the 1D wires (n_{1D}), the 1D Fermi wave vector k_F (all to about ±1%), and the ratio of the charge and the spin velocities at low energies (to about ±5%), extracted from the gradients of the S and C lines in Fig. 8, for different finger-gate voltages V_F.

V_F (V)	n_{2D} (10^{15} m^{-2})	n_{1D} (10^7 m^{-1})	k_F (10^7 m^{-1})	v_c/v_s
−0.60	1.67	5.68	8.9	1.5
−0.65	1.65	4.99	7.8	1.6
−0.68	1.52	4.79	7.5	1.5
−0.70	1.48	4.60	7.2	1.8

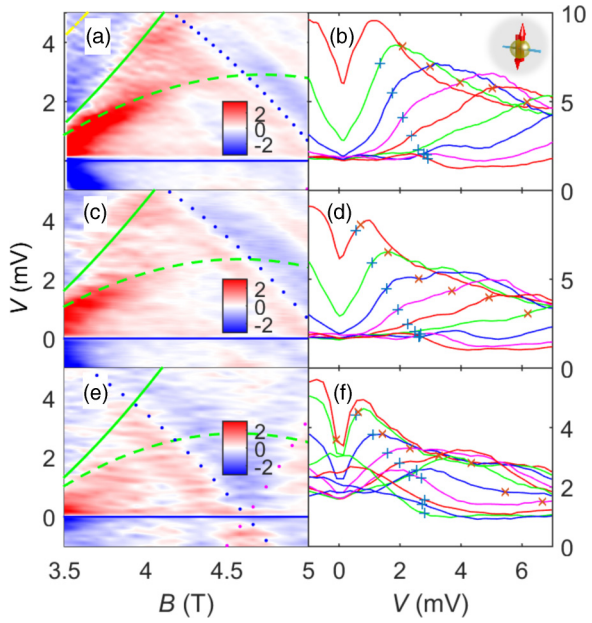

FIG. 9. (Left) Intensity plots of dG/dV (in μS/mV), for various finger-gate voltages and samples: [(a) and (b)] $V_F = -0.68$ V, $V_P = 0.2$ V, from Fig. 8(e), sample A, which had 10 μm-long wires ($T \sim 300$ mK); [(c) and (d)] $V_F = -0.70$ V, $V_P = 0.3$ V, from Fig. 8(i), sample A; [(e) and (f)] a similar single-subband result from sample B (18 μm-long wires, $T < 100$ mK). The replica feature just above k_F appears as a pale triangle (slowly varying G) between the two green curves, after a red region (sharp rise in G). The replica feature for sample B is somewhat weaker than that for sample A, in line with the wire-length dependence predicted in this paper. Right column: G vs V at various fields B from 3 to 4.8 T for the data in the matching plots in the left column; "+" and "×" symbols on each curve indicate, respectively, the voltages corresponding to the dashed and solid [$p1b$ and $p1a(l)$] green lines in the left column (and in Fig. 8), showing the enhanced conductance between the two.

the "p" parabolae using a gate above most of the "p" region, showing that the replica feature is independent of the "p" tunneling. The amplitude of the feature dies away rapidly, and beyond the "p" parabolae, we have measured up to 8 T with high sensitivity, but find no sign of any feature that can be distinguished from the decaying tails of the other features.

In the range of fields where the $p1b$ feature is observed its strength decreases as the B field increases away from the crossing point analogously to the power law for spinless fermions in Table I. On general grounds, it is natural to expect that divergence of the spectral weight of a b mode toward an a mode is a general feature, but there is no known method for performing a microscopic calculation in the spinful case. A similar feature should mark the $h0b(r)$ mode (see Fig. 3 and Table I) for negative voltages and for the magnetic field just below the crossing point k_F, but it would be very difficult to resolve due to the overlaying spin and charge lines.

Making an analogy with the microscopic theory for spinless fermions in the first part of this paper, we estimate the ratio of signals around different spectral edges using the 1D Fermi wavelength, $\lambda_F \approx 130$ nm for our samples, as the short-range scale $\mathcal{R}$. The signal from the principal parabola, see Fig. 8(b), gives the amplitude of the a mode as $G_a \approx 5\,\mu$S. Then the amplitude of the signal from the second (third)-level excitations is predicted to be smaller by a factor of more than $\lambda_F^2/L^2 \sim 2 \times 10^{-4}$ ($\lambda_F^4/L^4 = 3 \times 10^{-8}$), where the length of a wire is $L = 10\,\mu$m. These values $G_a\lambda_F^2/L^2 \sim 10^{-3}\,\mu$S ($G_a\lambda_F^4/L^4 \sim 10^{-7}\,\mu$S) are at least two orders of magnitude smaller than the background and noise levels of our experiment $G_{\text{noise}} \sim 10^{-2}\,\mu$S, which places an upper limit on the amplitude of any replica away from k_F. Thus our observations are consistent with the mode hierarchy picture for fermions.

In an effort to quantify the decay of the replica feature, we have fitted the gradual background fall in conductance and the noninteracting 1D and 2D peaks (solid green and blue lines in Figs. 7–9) with a Gaussian and/or Lorentzian functions of B, at each value of $V > 0$. The fitting parameters are then fitted to smooth functions in order to represent the general behavior of the peaks as a function of V. This idealized landscape is then subtracted from the data, see Fig. 10(a), and the "replica"

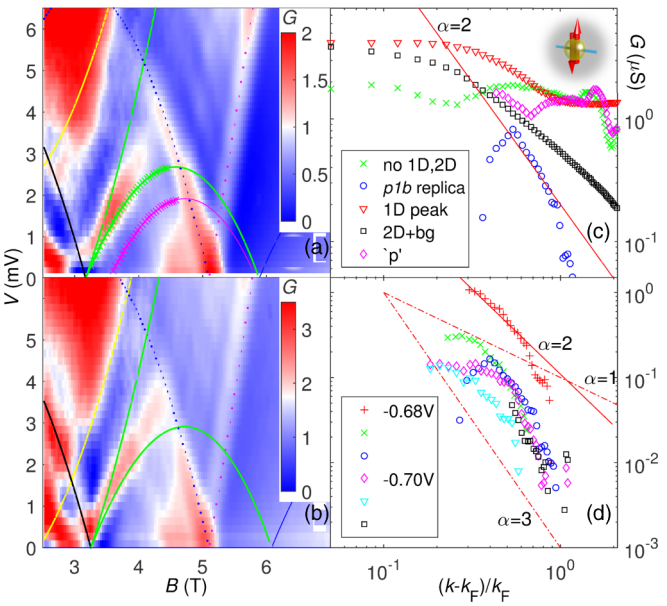

FIG. 10. (a) and (b) The conductance for $V_F = -0.70$ and -0.68 V, respectively, for sample A, after subtraction of an idealized landscape made up of fits or estimates of the noninteracting 1D-2D and "p" parabolae (see text). The $p1b$ replica is seen clearly as the red region of enhanced conductance. (c) The conductance along the $p1b$ replica parabola, for the data in (a) (green crosses). The conductance on $p1b$ has a large contribution from the "p" region [the line in (a) marked with blue dots, which is blurred to the left by multiple copies at slightly different positions]. In order to correct for this contribution, the conductance along a matching parabola shifted along the dotted "p" line in (a) (shown as a dashed magenta line there), is subtracted from the $p1b$ data. This yields the points marked with blue circles, which appears to be nonzero because of the enhancement at $p1b$. The amplitude decays rapidly. There are many uncertainties in the fitting of the other peaks, but the replica appears clearly and the decay of the conductance is consistent with an inverse-square power law $G \propto (k - k_F)^{-\alpha}$ (labelled $\alpha = 2$), which is the behavior predicted by the theory for $k > k_F + \gamma$ where $\gamma \ll k_F$ (see Table I). (d) The $p1b$ conductance enhancement as shown with circles in (b). Three different methods of fitting the background and the 1D and 2D peaks are compared for each of two gate voltages as shown. The curves are offset vertically for clarity. The lines marked with values of α are guides to the eye. The data are all consistent with $\alpha = 2 \pm 1$.

is then fairly easily observed in the remaining conductance. A copy of a nearby region along the "p" curve is then subtracted too, as an approximation to the rather diffuse signal arising from the main "p" peak and smaller versions of it at slightly different densities. This also reduces errors in the peak and background fitting used in (a). We then plot the conductance along the expected parabola [dashed line in (a)] as a function of $(k-k_{\rm F})/k_{\rm F} = (B-B_+)/((B_+-B_-)/2)$. These data are shown as circles in (c), where all the other contributions to the conductance along the same parabola are shown. Here, $B_+ = 3.17$ T and $k_{\rm F} = 7.2\times 10^7$ m^{-1}. It is very hard to be sure that this procedure is reliable due to significant error bars imposed by contributions from the various other peaks, but it is clear that the replica feature dies away rapidly as a function of $k-k_{\rm F}$, and it is consistent with the $1/(k-k_{\rm F})^2$ law predicted for $p1b$ in Table I for $k-k_{\rm F}\gg\gamma$. Though the overall prefactor is unknown theoretically in the spinful case, this singular power law may overcome the reduction factor $\mathcal{R}^2/L^2$ close to $k_{\rm F}$.

IX. CONCLUSIONS

In this work, we have shown that a hierarchy of modes emerges in systems of interacting fermions in one dimension at high energy controlled by the system length, in marked contrast to the well-known fermionic quasiparticles of a Fermi liquid and hydrodynamic modes of a Luttinger liquid at low energy. We have obtained theoretically the dynamic response functions for a model of spinless fermions with short-range interactions using the exact diagonalisation methods of the Bethe ansatz for the spectrum and the form factors of the system. Analysing the spectral function in detail, we have found that the first-level (strongest) mode in long systems has a parabolic dispersion, like that of a renormalized free particle. The second-level excitations produce a singular power-law line shape for the first-level mode and different kinds of power-law behavior at the spectral edges. Evaluating the form factor necessary for the dynamical structure factor we have shown that it has the same general form as the form factor of the spectral function, manifesting the same hierarchy of modes.

Using the same many-body matrix elements obtained microscopically, we have also calculated the local density of states. It provides a more convenient way to analyze how the hierarchy at high energy changes into the hydrodynamic modes of the Luttinger liquid at low energies. We have shown, via a full Bethe-ansatz calculation, that the LDOS is suppressed at the Fermi energy in a power-law fashion in full accord with the prediction of the Tomonaga-Luttinger model. Away from the Fermi point, where the Lorentz invariance of the linear dispersion is reduced to Galilean by the parabolicity of the spectrum, the LDOS is dominated by the first (leading) level of the hierarchy. We have demonstrated that the transition from one regime to another is a smooth crossover.

We measure momentum-resolved tunneling conductance in one-dimensional wires formed in the GaAs/AlGaAs double-well heterostructure by an array of finger gates. In this setup, we probe the spectral function of unpolarized electrons (spinful fermions) and find a pronounced spin-charge separation at low energy with a ratio of the spin and the charge velocities up to 1.8, which confirms that our system is in the strongly interacting regime. By varying the gate voltage that controls the width of our 1D wires, we demonstrate control of the interaction strength of about 20%; the deeper confining potential of the wires populates higher 1D subbands as well which in turn screens stronger Coulomb interactions in the principal 1D band reducing the interaction strength. In 10 μm-long wires, we find a clear feature resembling the second-level excitations, which dies away rapidly at high momentum. A qualitative fit shows that the feature decays in a fashion that is consistent with the power-law prediction in this paper for spinless electrons. Thus we have shown that the hierarchy is apparently a generic phenomenon at least for one- and two-point correlation functions of fermions without spin, and for a transport experiment for fermions with spin.

Data associated with this work are available from [50].

ACKNOWLEDGMENTS

We acknowledge financial support from the UK EPSRC through Grants No. EP/J01690X/1 and No. EP/J016888/1 and from the DFG through SFB/TRR 49. This research was supported in part by the National Science Foundation under Grant No. NSF PHY11-25915.

APPENDIX A: EIGENVALUE EQUATION IN THE ALGEBRAIC FRAMEWORK

The eigenvalue of the transfer matrix $\tau(u)$ in Eq. (19) can be evaluated using the commutation relations in Eqs. (16) and (17). Let Ψ be a Bethe state in the algebraic representation of Eq. (21). The results of acting with $A(u)$ and $D(u)$ operators on the state Ψ are obtained by commuting these operators from left to right though the product of $C(u_j)$ in Eq. (21) and then by using their vacuum eigenvalues in Eq. (20).

Let us consider the case of $N=2$ and the operator $A(u)$ first. Commuting once by means of Eq. (16) gives

$$A(u)C(u_2)C(u_1)|0\rangle = \left(\frac{1}{b(u_2-u)}C(u_2)A(u) - \frac{c(u_2-u)}{b(u_2-u)}C(u)A(u_2)\right)C(u_1)|0\rangle. \tag{A1}$$

Applying Eq. (16) the second time gives

$$\begin{aligned} A(u)C(u_2)C(u_1)|0\rangle = &\left(\frac{1}{b(u_2-u)}\frac{1}{b(u_1-u)}C(u_2)C(u_1)a(u) - \frac{c(u_1-u)}{b(u_1-u)}\frac{1}{b(u_2-u)}C(u_2)C(u)a(u_1)\right)|0\rangle \\ &+\left(-\frac{1}{b(u_1-u_2)}\frac{c(u_2-u)}{b(u_2-u)}C(u)C(u_1)a(u_2) + \frac{c(u_1-u_2)}{b(u_1-u_2)}\frac{c(u_2-u)}{b(u_2-u)}C(u)C(u_2)a(u_1)\right)|0\rangle, \end{aligned} \tag{A2}$$

where the vacuum eigenvalue of $A(u)$, $A(u)|0\rangle = a(u)|0\rangle$, was substituted explicitly. The second terms in the first and the second lines of the above equation have the same operator form but different scalar factors. Summation of the two scalar factor, using the explicit form of $b(u)$ and $c(u)$ from Eq. (12), yields

$$\frac{a(u_1)}{b(u_2-u)}\left[\frac{c(u_1-u_2)}{b(u_1-u_2)}c(u_2-u)-\frac{c(u_1-u)}{b(u_1-u)}\right]=-\frac{a(u_1)}{b(u_2-u_1)}\frac{c(u_1-u)}{b(u_1-u)}. \tag{A3}$$

Thus the four terms can be rewritten as only three terms,

$$A(u)C(u_2)C(u_1)|0\rangle=\left(a(u)\prod_{j=1}^{2}\frac{C(u_j)}{b(u_j-u)}-\sum_{j=1}^{2}a(u_j)\frac{c(u_j-u)}{b(u_j-u)}C(u)\prod_{l=1\neq j}^{2}\frac{C(u_l)}{b(u_l-u_j)}\right)|0\rangle. \tag{A4}$$

Extension of the same procedure for $N>2$ gives

$$A(u)\prod_{j=1}^{N}C(u_j)|0\rangle=\left(a(u)\prod_{j=1}^{N}\frac{1}{b(u_j-u)}C(u_j)-\sum_{j=1}^{N}a(u_j)\frac{c(u_j-u)}{b(u_j-u)}C(u)\prod_{l=1\neq j}^{N}\frac{1}{b(u_l-u_j)}C(u_l)\right)|0\rangle \tag{A5}$$

Commuting of the operator $D(u)$ is done in the same way using Eq. (17) and yields

$$D(u)\prod_{j=1}^{N}C(u_j)|0\rangle=\left(d(u)\prod_{j=1}^{N}\frac{-1}{b(u-u_j)}C(u_j)+\sum_{j=1}^{N}d(u_j)\frac{c(u-u_j)}{b(u-u_j)}C(u)\prod_{l=1\neq j}^{N}\frac{-1}{b(u_j-u_l)}C(u_l)\right)|0\rangle. \tag{A6}$$

Thus a Bethe state in Eq. (21) parametrized by an arbitrary set of u_j is not an eigenstate of the transfer matrix since acting of the operator $\tau(u)$ on such a state does not only result in multiplying by a scalar but also generates many different states: the second terms in Eqs. (A5) and (A6). However, the coefficients in front of each of these extra states can be made zero by a specific choice of u_j,

$$a(u_j)\prod_{l=1\neq j}^{N}\frac{1}{b(u_l-u_j)}-d(u_j)\prod_{l=1\neq j}^{N}\frac{-1}{b(u_j-u_l)}=0. \tag{A7}$$

When a set of u_j satisfies the system of equations above, the corresponding Bethe state is an eigenstate of the transfer matrix, $\tau(u)\Psi=\mathcal{T}(u)\Psi$, with the eigenvalue $\mathcal{T}$ given by the first terms in Eqs. (A5) and (A6),

$$\mathcal{T}(u)=a(u)\prod_{j=1}^{N}\frac{1}{b(u_j-u)}-d(u)\prod_{j=1}^{N}\frac{-1}{b(u-u_j)}. \tag{A8}$$

Equation (A7) is the set of Bethe equations in the algebraic representation, Eq. (22) of the main part of the text, and Eq. (A8) gives the eigenvalue of the transfer matrix, Eq. (24) of the main part of the text.

APPENDIX B: CALCULATION OF AVERAGES OF THE LOCAL DENSITY OPERATOR $\rho(0)$

The calculation of the average of the local density operator $\rho(0)$ is done in the same way as for the field operator $\psi^{\dagger}(0)$ in Sec. IV C. We start from the lattice model in Eq. (2) and the corresponding construction of the algebraic Bethe ansatz in Sec. IV A.

The local density operator can be represented in terms of A and D operators as [17,18]

$$\rho_1=-D\left(\frac{i\pi}{2}-\eta\right)\tau\left(\frac{i\pi}{2}-\eta\right)^{\mathcal{L}-1}. \tag{B1}$$

The action of the second factor in the above expression on an eigenstate $|\mathbf{u}\rangle$ just gives a phase factor—see an explanation after Eq. (31)—that we will ignore since we are interested in the modulus squared of this form factor. Then commuting the operator D of the first factor in the equation above through all C operators of the eigenstate $|\mathbf{u}\rangle$—in the form in Eq. (21)—gives the result in Eq. (A6).

The scalar product of Eq. (A6), where the auxiliary parameter u is set to $i\pi/2-\eta$, with another eigenstate $\langle\mathbf{v}|$ gives

$$\langle\mathbf{v}|\rho_1|\mathbf{u}\rangle=(-1)^N\prod_{j=1}^{N}\frac{\cosh\left(u_j-\eta\right)}{\cosh\left(u_j+\eta\right)}\langle\mathbf{u}|\mathbf{v}\rangle+i(-1)^N\sum_{b=1}^{N}\frac{\sinh 2\eta}{\cosh\left(u_b+\eta\right)}\prod_{l=1\neq b}^{N}\frac{\sinh\left(u_b-u_l+2\eta\right)}{\sinh\left(u_b-u_l\right)}\left\langle u_{b-1},\frac{i\pi}{2}-\eta,u_{b+1}|\mathbf{v}\right\rangle, \tag{B2}$$

where $\langle u_{b-1},\frac{i\pi}{2}-\eta,u_{b+1}|$ is a Bethe state which is constructed from the eigenstate $\mathbf{u}$ by replacing bth quasimomenta with $i\pi/2-\eta$. Note that the properties $\langle\mathbf{v}|\mathbf{u}\rangle=\langle\mathbf{u}|\mathbf{v}\rangle$, where u_j satisfy the Bethe equations and v_j is an arbitrary set of quasimomenta [17,18], was used.

The scalar product in the first line in Eq. (B2) is given by Eqs. (27) and (28) where $\mathbf{u}$ and $\mathbf{v}$ are swapped. Substitution of $\mathbf{u} = u_{b-1}, \frac{i\pi}{2} - \eta, u_{b+1}$ in the same expressions for the scalar products in the second line of Eq. (B2) yields

$$\left\langle u_{b-1}, \frac{i\pi}{2} - \eta, u_{b+1} | \mathbf{v} \right\rangle = -i \frac{\sinh^N(2\eta) \prod_{j=1}^N \cosh(v_j - \eta) \det \hat{T}^{(b)}}{\prod_{j<i} \sinh(v_j - v_i) \prod_{j<i\neq b} \sinh(u_j - u_i)(-1)^{b-1} \prod_{j=1\neq b}^N \cosh(u_j + \eta)}, \tag{B3}$$

where all matrix elements of $\hat{T}^{(b)}$ are

$$T^{(b)}_{ab'} = \prod_{l=1\neq b'}^N \frac{\sinh(u_{b'} - u_l + 2\eta)}{\sinh(u_{b'} - u_l - 2\eta)} \frac{1}{\sinh(u_{b'} - v_a)} \prod_{j=1\neq a}^N \sinh(u_{b'} - v_j - 2\eta) - \frac{1}{\sinh(u_{b'} - v_a)} \prod_{j=1\neq a}^N \sinh(u_{b'} - v_j + 2\eta) \tag{B4}$$

for $b' \neq b$

$$\hat{T}^{(b)}_{ab'} = \frac{1}{\cosh(v_a + \eta)\cosh(v_a - \eta)} \tag{B5}$$

for $b' = b$.

After pulling a common factor out of the brackets in Eq. (B2) and absorbing the b-dependent prefactors in front of the determinants in the second line of Eq. (B2) into the bth columns of the matrices under the determinants, the form factor in Eq. (B2) reads as

$$\langle \mathbf{v}|\rho_1|\mathbf{u}\rangle = \prod_{j=1}^N \frac{\cosh(u_j - \eta)}{\cosh(u_j + \eta)} \frac{\sinh^N(2\eta)}{\prod_{j<i} \sinh(v_j - v_i) \prod_{j<i} \sinh(u_j - u_i)} \left[\det \hat{T} + \sum_{b=1}^N \det \hat{\tilde{T}}^{(b)} \right]. \tag{B6}$$

Here the matrix elements of $\hat{\tilde{T}}^{(b)}$, which are obtain by multiplying by the corresponding scalars, are

$$\tilde{T}^{(b)}_{ab'} = \prod_{l=1\neq b'}^N \frac{\sinh(u_{b'} - u_l + 2\eta)}{\sinh(u_{b'} - u_l - 2\eta)} \frac{1}{\sinh(u_{b'} - v_a)} \prod_{j=1\neq a}^N \sinh(u_{b'} - v_j - 2\eta) - \frac{1}{\sinh(u_{b'} - v_a)} \prod_{j=1\neq a}^N \sinh(u_{b'} - v_j + 2\eta) \tag{B7}$$

for $b' \neq b$

$$\tilde{T}^{(b)}_{ab'} = (-1)^N \prod_{l=1\neq b'}^N \sinh(u_{b'} - u_l + 2\eta) \prod_{j=1}^N \frac{\cosh(v_j - \eta)}{\cosh(u_j - \eta)} \frac{\sinh(2\eta)}{\cosh(v_a + \eta)\cosh(v_a - \eta)} \tag{B8}$$

for $b' = b$. Note that $\tilde{T}^{(b)}_{ab'} = T_{ab'}$ for $b' \neq b$.

Finally, the summation over b in Eq. (B6) can be evaluated using a general matrix identity: $\det \hat{T} + \sum_{b=1}^N \det \hat{\tilde{T}}^{(b)} = \det(\hat{T} + \hat{B})$, where $\hat{\tilde{T}}^{(b)}$ is obtained from the matrix $\hat{T}$ by substituting bth column from matrix $\hat{B}$. After constructing the matrix $\hat{B}$ out matrix elements $\tilde{T}^{(b)}_{ab}$ from Eq. (B8) and performing the summation over b in Eq. (B6), the form factor reads

$$\langle \mathbf{v}|\rho_1|\mathbf{u}\rangle = \prod_{j=1}^N \frac{\cosh(u_j - \eta)}{\cosh(u_j + \eta)} \frac{\sinh^N(2\eta)}{\prod_{j<i} \sinh(v_j - v_i) \prod_{j<i} \sinh(u_j - u_i)} \det \hat{K}, \tag{B9}$$

where the matrix elements of $\hat{K}$ are

$$\begin{aligned} K_{ab} = &\prod_{l=1\neq b}^N \frac{\sinh(u_b - u_l + 2\eta)}{\sinh(u_b - u_l - 2\eta)} \frac{1}{\sinh(u_b - v_a)} \prod_{j=1\neq a}^N \sinh(u_b - v_j - 2\eta) - \frac{1}{\sinh(u_b - v_a)} \prod_{j=1\neq a}^N \sinh(u_b - v_j + 2\eta) \\ &+ (-1)^N \prod_{l=1\neq b}^N \sinh(u_b - u_l + 2\eta) \prod_{j=1}^N \frac{\cosh(v_j - \eta)}{\cosh(u_j - \eta)} \frac{\sinh(2\eta)}{\cosh(v_a + \eta)\cosh(v_a - \eta)}. \end{aligned} \tag{B10}$$

Now, we evaluate the long-wavelength limit for the result above. Applying the inversion mapping from the algebraic to the coordinate representation from Eq. (35) to the matrix elements in Eq. (B10) and expanding the result up to the leading order $k^u_j, k^v_j \ll 1$, we obtain

$$K_{ab} = (-1)^{N-1} 2mU((mU)^2 - 1)^{\frac{N-2}{2}} \frac{\sum_{j=1}^N k^v_j - \sum_{j=1}^N k^u_j - k^v_a + k^u_a}{k^u_b - k^v_a} + 2(mU + 1)((mU)^2 - 1)^{\frac{N-2}{2}}. \tag{B11}$$

Repeating the same procedure for the prefactor in Eq. (B9) and pulling a common scalar factor out of the matrix elements under the determinant, we obtain

$$\langle \mathbf{v}|\rho(0)|\mathbf{u}\rangle = (-1)^{N^2} 2^N \frac{(mU)^N}{(mU+1)^N} (mU-1)^{N^2} \det \hat{\mathcal{K}}, \tag{B12}$$

where the matrix elements of $\hat{\mathcal{K}}$ are

$$\mathcal{K}_{ab} = \frac{k_a^u - k_a^v - \Delta P}{k_b^u - k_a^v} + (-1)^{N-1} \frac{mU+1}{mU}, \tag{B13}$$

and $\Delta P = \sum_{j=1}^N k_j^u - \sum_{j=1}^N k_j^v$.

Evaluating the determinant, we obtain

$$\det \mathcal{K} = \frac{mU+1}{mU} \frac{(\Delta P)^N \prod_{i<j} \left(k_i^u - k_j^u\right) \prod_{i<j} \left(k_i^v - k_j^v\right)}{\prod_{i,j} \left(k_i^u - k_j^v\right)}. \tag{B14}$$

This formula can be proved by induction analogously to the proof of Eq. (43).

The form factor appearing in the dynamical structure factor in Eq. (10) is a modulus squared of Eq. (B12). Normalizing the initial and the finial states using Eq. (38) as $|\langle f|\rho(0)|0\rangle|^2 = |\langle \mathbf{k}^f|\rho(0)|\mathbf{k}^0\rangle|^2 \langle \mathbf{k}^f|\mathbf{k}^f\rangle^{-1} \langle \mathbf{k}^0|\mathbf{k}^0\rangle^{-1}$, we obtain

$$|\langle f|\rho(0)|0\rangle|^2 = \frac{(mU)^{2N-2}}{(mU+1)^{2N-2}} \frac{P_f^{2N} \prod_{i<j}^N \left(k_i^0 - k_j^0\right)^2 \prod_{i<j}^N \left(k_i^f - k_j^f\right)^2}{\left(\mathcal{L} - \frac{NmU}{1+mU}\right)^{2N} \prod_{i,j=1}^N \left(k_i^0 - k_j^f\right)^2}, \tag{B15}$$

where $P_0 = 0$ for the ground state. Equation (B15) is Eq. (47) in the main part of the text with $Z = mU/(mU+1)/(\mathcal{L} - NmU/(1+mU))$.

Note that when the final state becomes the ground state, $\mathbf{k}^f = \mathbf{k}^0$, Eq. (B15) is divergent. In this case, the matrix element is evaluated using only translational symmetry and the definition of the number of particles operator as

$$|\langle f|\rho(0)|0\rangle|^2 = \frac{N^2}{\mathcal{L}^2}, \tag{B16}$$

which also follows directly from Eqs. (B9) and (B10), by taking the limit $\mathbf{v} \to \mathbf{u}$.

[1] P. Nozières, *Theory of Interacting Fermi Systems* (Addison-Wesley, New York, 1997).

[2] T. Giamarchi, *Quantum Physics in One Dimension* (Clarendon press, Oxford, 2003).

[3] B. Roulet, J. Gavoret, and P. Nozières, Phys. Rev. **178**, 1072 (1969).

[4] P. Nozières, J. Gavoret, and B. Roulet, Phys. Rev. **178**, 1084 (1969).

[5] P. Nozières and C. T. de Dominicis, Phys. Rev. **178**, 1097 (1969).

[6] A. Imambekov, T. L. Schmidt, and L. I. Glazman, Rev. Mod. Phys. **84**, 1253 (2012).

[7] O. Tsyplyatyev, A. J. Schofield, Y. Jin, M. Moreno, W. K. Tan, C. J. B. Ford, J. P. Griffiths, I. Farrer, G. A. C. Jones, and D. A. Ritchie, Phys. Rev. Lett. **114**, 196401 (2015).

[8] N. A. Slavnov, Theor. Math. Phys. **79**, 502 (1989).

[9] O. Tsyplyatyev and A. J. Schofield, Phys. Rev. B **90**, 014309 (2014).

[10] G. Barak, H. Steinberg, L. N. Pfeiffer, K. W. West, L. Glazman, F. von Oppen, and A. Yacoby, Nat. Phys. **6**, 489 (2010).

[11] O. M. Auslaender, A. Yacoby, R. de Picciotto, K. W. Baldwin, L. N. Pfeiffer, and K. W. West, Science **295**, 825 (2002).

[12] Y. Jompol, C. J. B. Ford, J. P. Griffiths, I. Farrer, G. A. C. Jones, D. Anderson, D. A. Ritchie, T. W. Silk, and A. J. Schofield, Science **325**, 597 (2009).

[13] V. E. Korepin, N. M. Bogoliubov, and A. G. Izergin, *Quantum Inverse Scattering Methods and Correlation Functions* (Cambridge University Press, Cambridge, 1993).

[14] F. D. M. Haldane, Phys. Lett. A **81**, 153 (1981).

[15] J. von Delft and H. Schoeller, Ann. Phys. **7**, 225 (1998).

[16] A. A. Abrikosov, L. P. Gorkov, and I. E. Dzyaloshinski, *Methods of Quantum Field Theory in Statistical Physics* (Dover, New York, 1975).

[17] N. Kitanine, J. M. Maillet, and V. Tetras, Nucl. Phys. B **554**, 647 (1999).

[18] N. Kitanine and J. M. Maillet, Nucl. Phys. B **567**, 554 (2000).

[19] P. Jordan and E. Wigner, Zeitschrift fur Physik **47**, 631 (1928).

[20] J. M. Maillet and J. Sanchez de Santos, Amer. Math. Soc. Trause. **201**(2), 137 (2000), arXiv:q-alg/9612012.

[21] V. G. Drinfeld, Doklady Akademii Nauk SSSR **273**, 531 (1983) [Sov. Math. Dokl. **28**, 667 (1983)].

[22] F. Gohmann and V. E. Korepin, J. Phys. A **33**, 1199 (2000).

[23] K. Motegi and K. Sakai, Nucl. Phys. B **793**, 451 (2008).

[24] M. Gaudin, B. M. McCoy, and T. T. Wu, Phys. Rev. D **23**, 417 (1981).

[25] J.-S. Caux and J. M. Maillet, Phys. Rev. Lett. **95**, 077201 (2005).

[26] J.-S. Caux, R. Hagemans, and J. M. Maillet, J. Stat. Mech. (2005) P09003.

[27] J.-S. Caux, P. Calabrese, and N. Slavnov, J. Stat. Mech. (2007) P01008.

[28] R. G. Pereira, J. Sirker, J.-S. Caux, R. Hagemans, J. M. Maillet, S. R. White, and I. Affleck, Phys. Rev. Lett. **96**, 257202 (2006).
[29] R. G. Pereira, S. R. White, and I. Affleck, Phys. Rev. B **79**, 165113 (2009).
[30] J. Links, H.-Q. Zhou, R. H. McKenzie, and M. D. Gould, J. Phys. A **36**, R63 (2003).
[31] D. Biegel, M. Karbach, and G. Muller, Europhys. Lett. **59**, 882 (2002).
[32] D. Biegel, M. Karbach, and G. Muller, J. Phys. A **36**, 5361 (2003).
[33] J. Sato, M. Shiroishi, and M. Takahashi, J. Phys. Soc. Jpn. **73**, 3008 (2004).
[34] M. Pustilnik, M. Khodas, A. Kamenev, and L. I. Glazman, Phys. Rev. Lett. **96**, 196405 (2006),
[35] M. Khodas, M. Pustilnik, A. Kamenev, and L. I. Glazman, Phys. Rev. B **76**, 155402 (2007).
[36] A. Imambekov and L. I. Glazman, Phys. Rev. Lett. **102**, 126405 (2009).
[37] A. Imambekov and L. I. Glazman, Science **323**, 228 (2009).
[38] O. M. Auslaender, H. Steinberg, A. Yacoby, Y. Tserkovnyak, B. I. Halperin, K. W. Baldwin, L. N. Pfeiffer, and K. W. West, Science **308**, 88 (2005).
[39] Y. Tserkovnyak, B. I. Halperin, O. M. Auslaender, and A. Yacoby, Phys. Rev. B **68**, 125312 (2003).
[40] M. Khodas, M. Pustilnik, A. Kamenev, and L. I. Glazman, Phys. Rev. Lett. **99**, 110405 (2007).
[41] R. G. Pereira, J. Sirker, J.-S. Caux, R. Hagemans, J. M. Maillet, S. R. White, and I. Affleck, J. Stat. Mech. (2007) P08022.
[42] A. Imambekov and L. I. Glazman, Phys. Rev. Lett. **100**, 206805 (2008).
[43] A. Kamenev and L. I. Glazman, Phys. Rev. A **80**, 011603 (2009).
[44] T. L. Schmidt, A. Imambekov, and L. I. Glazman, Phys. Rev. Lett. **104**, 116403 (2010).
[45] T. L. Schmidt, A. Imambekov, and L. I. Glazman, Phys. Rev. B **82**, 245104 (2010).
[46] F. H. L. Essler, Phys. Rev. B **81**, 205120 (2010).
[47] O. Tsyplyatyev and A. J. Schofield, Phys. Rev. B **88**, 115142 (2013).
[48] A. Altland, C. H. W. Barnes, F. W. J. Hekking, and A. J. Schofield, Phys. Rev. Lett. **83**, 1203 (1999).
[49] B. Kardynal, C. H. W. Barnes, E. H. Linfield, D. A. Ritchie, K. M. Brown, G. A. C. Jones, and M. Pepper, Phys. Rev. Lett. **76**, 3802 (1996).
[50] https://www.repository.cam.ac.uk/handle/1810/254193.